Uncertainties in Coastal Ocean Color Products: Impacts of Spatial Sampling

Nima Pahlevan[a,b], Sudipta Sarkar[a,b], Bryan A. Franz[a]

[a]NASA Goddard Space Flight Center, 8800 Greenbelt Rd, Greenbelt, MD, 20771

[b]Science Systems and Applications, Inc., 10210 Greenbelt Rd, Suite 600, Lanham, MD 20706

ABSTRACT

With increasing demands for ocean color (OC) products with improved accuracy and well characterized, per-retrieval uncertainty budgets, it is vital to decompose overall estimated errors into their primary components. Amongst various contributing elements (e.g., instrument calibration, atmospheric correction, inversion algorithms) in the uncertainty of an OC observation, less attention has been paid to uncertainties associated with spatial sampling. In this paper, we simulate MODIS and VIIRS OC products from 30m resolution OC products derived from the Operational Land Imager (OLI) aboard Landsat-8, to examine impacts of spatial sampling on both cross-sensor product intercomparisons and in-situ validations of R_{rs} products in coastal waters. The simulations were carried out for OLI scenes "scanned" for one full orbital-repeat cycle of each ocean color satellite. While some view-angle dependent differences in simulated Aqua-MODIS and VIIRS were observed, the average uncertainties (absolute) in product intercomparisons (due to differences in spatial sampling) at regional scales are found to be 1.8%, 1.9%, 2.4%, 4.3%, 2.7%, 1.8%, and 4% for the $R_{rs}(443)$, $R_{rs}(482)$, $R_{rs}(561)$, $R_{rs}(655)$, [Chla], $K_d(482)$, and $b_{bp}(655)$ products, respectively. It is also found that, depending on in-water spatial variability and the sensor's footprint size, the errors for an

in-situ validation location in coastal areas can reach as high as $\pm 18\%$. We conclude that a) expected biases induced by the spatial sampling in product intercomparisons are mitigated when products are averaged over at least $7km \times 7km$ windows, b) VIIRS observations, with improved consistency in cross-track spatial sampling yields more precise calibration/validation results than MODIS, and c) use of a single pixel centered on in-situ coastal sites provides an optimal sampling size for validation efforts. These findings will have implications for enhancing our understanding of uncertainties in ocean color retrievals and for planning of future calibration/validation exercises.

1. INTRODUCTION

Following four decades of research and development, ocean color (OC) products from spaceborne remote sensing instruments now play a critical role in the management and monitoring of coastal ecosystems, which are under increased stress due to human population growth in coastal areas and associated anthropogenic impacts such as pollution and agricultural run-off (McGranahan et al. 2007; Nixon 1995; Vitousek et al. 1997; Vörösmarty et al. 2000). Repeatable, timely, and reliable OC products provide a viable and efficient tool for monitoring of these coastal ecosystems. Coastal OC products provide a synoptic view of coastal ecosystems at an instance of time and when assimilated with coupled hydrodynamic-ecosystem coastal models (Allen et al. 2008; Gohin et al. 2005; IOCCG 1997; Natvik and Evensen 2003; Ouillon et al. 2004) allow for nowcasting and forecasting of environmental conditions to aid in hazard mitigation efforts (e.g., occurrence of harmful algal blooms). Within the suite of OC products distributed by NASA, the remote sensing reflectance (R_{rs}; defined as the ratio of water-

49 leaving radiance and the total downwelling irradiance just above the surface) plays a
50 central role in determining the optical and biogeochemical properties of coastal oceans.
51 These observations and products, however, come from various satellite sensors with
52 known, partially known, or unknown uncertainties in their radiometric observations or
53 derived geophysical products. These sensors and their processing approaches are
54 managed by various space agencies (http://www.ioccg.org), and despite international
55 efforts to coordinate satellite ocean color programs (e.g., http://ceos.org), the derived
56 products can be expected to differ due to uncertainties associated with sensor design and
57 calibration and geophysical retrieval algorithms. Examples of satellite ocean color
58 sensors are the Sea-viewing Wide Field-of-view Sensor onboard Orbview-2 (McClain et
59 al. 2004; O'Reilly et al. 1998), the Moderate Resolution Imaging Spectroradiometer
60 (MODIS) onboard both Aqua and Terra platforms (Esaias et al. 1998), and the recently
61 launched Visible Infrared Imaging Radiometer Suite (VIIRS) onboard the Suomi
62 National Preparatory Partnership (SNPP). To ensure climate-quality products and
63 consistent data record, the OC products are validated against in-situ observations, and
64 individual satellite records are compared over their common mission overlapping periods.
65 Each of these comparison methods carries unique uncertainties.
66 The in-situ R_{rs} measurements are commonly made during research cruises or at
67 stationary field stations (Antoine et al. 2008a; Zibordi et al. 2009a; Zibordi et al. 2009b).
68 The ocean color component of the AErosol RObotic NETwork (AERONET-OC) is a
69 good example of an internationally coordinated automated network of radiometric
70 observations in coastal areas (Zibordi et al. 2009b). The sources of uncertainties in such
71 field validation efforts are attributed to a) the instrument calibration (Antoine et al.

72 2008a; Clark et al. 1997; Mueller et al. 2004), b) the post-processing techniques (Zibordi
73 et al. 2004), c) differences in the spectral sampling of the in-situ instruments and that of
74 the OC sensor (Wang 1999), and d) the spatial representativeness of the in-situ
75 observation (Mélin and Franz 2014).

76 The uncertainty in intercomparisons of OC-derived R_{rs} products, however,
77 corresponds to a) the sensors' radiometric performance on-orbit and the strategies
78 employed for vicarious calibration (Bailey et al. 2008; Franz et al. 2007; Zibordi et al.
79 2015) b) the atmospheric correction (Gordon 1997; Müller et al. 2015), c) differences in
80 spectral/spatial sampling, and d) the observation characteristics, i.e., angular
81 dependencies, including bidirectional reflectance distribution function (BRDF) effects
82 (Meister et al. 2012; Morel et al. 2002; Morel and Gentili 1996). This is further
83 complicated if a higher-level product intercomparison (e.g., chlorophyll-a, inherent
84 optical properties) is desired (Lee et al. 2010; Wang et al. 2005). The OC products
85 obtained from different sensors are often compared either over open oceans (Franz et al.
86 2005; Hu et al. 2013) or coastal waters (Barnes and Hu 2015; Hu and Le 2014; Ladner et
87 al. 2014; Mélin et al. 2011) to examine consistency amongst satellite observations and
88 detect any abnormal trending. In addition, various techniques have been proposed to
89 merge (fuse) different OC products (Maritorena et al. 2010; Maritorena and Siegel 2005;
90 Mélin et al. 2011; Mélin et al. 2009) to build comprehensive datasets less prone to spatial
91 and temporal gaps.

92 Among the sources of uncertainties for in-situ OC product validations (or calibration)
93 and cross-sensor intercomparisons, less attention has been paid to the characterization of
94 the impact of inherent in-water spatial variability and its relevance to sensors' spatial

95 sampling. Instead, efforts have been made to avoid or minimize the impact of spatial
96 sampling through various statistical analyses (Bailey and Werdell 2006; Mélin et al.
97 2007; Moore et al. 2015). One possible reason for the lack of prior research on the
98 uncertainties induced by differences in spatial sampling is the inability to decompose the
99 bulk uncertainty/bias into its components noted above. Bailey and Werdell (2006)
100 suggested performing a statistical test within 5×5-pixel boxes centered on the in-situ
101 matchups, where the coefficient of variation (CV; the ratio of standard deviation and
102 mean) of valid pixels is evaluated. Some other researchers have reported use of 3×3-
103 pixel boxes to analyze spatial variability at coastal sites (Zibordi et al. 2009a). Zibordi et
104 al. (2006) asserted that the error in the representativeness of in-situ measurements could
105 generally be treated as a random error, which can be minimized by increasing the sample
106 numbers and averaging over time. The statistical variability observed in this manner is a
107 combination of spatial variability and temporal variability, where the latter may be
108 associated with the instrument calibration or algorithm errors. A common uncertainty
109 goal for ocean color missions is to retrieve remote sensing reflectance with accuracies
110 better than 5% in the blue channels over the open ocean (Hooker et al. 1992).
111 Nevertheless, the reported biases for different coastal systems range from ±2% to ±35%
112 in R_{rs} products (Moore et al. 2015; Zibordi et al. 2009a; Zibordi et al. 2012). Moore et al.
113 (2015) reported bias values (for SeaWiFS and Aqua MODIS) larger than those published
114 in Zibordi et al. (2012) over optically complex waters. The appreciable discrepancies in
115 the results were due to the differences in the quality-control of the in-situ matchups.
116 Zibordi et al. (2012) showed that the differences in R_{rs} products (satellite-derived versus
117 in-situ) increase with the increase in the solar zenith angles and aerosol optical thickness.

118 Furthermore, the Group on Earth Observations (GEO), the Committee on Earth
119 Observation Systems (CEOS) and its working groups, together with the International
120 Ocean Colour Coordinating Group (IOCCG) are leading efforts in providing traceable
121 measurements with associated uncertainties to the user community. For a full treatment
122 of the error budget, it is desired that the uncertainties be specified at the component level,
123 i.e., instrument, atmospheric correction, spectral/spatial sampling error, inversion
124 algorithm errors, etc. For instance, for in-situ validations, both in-situ instruments
125 (Antoine et al. 2008a; Hooker and Maritorena 2000) and the OC sensor should have
126 traceable, and meaningful total uncertainty budget (Chander et al. 2013).
127 The present research provides a full and unique analysis of the impact of sensors'
128 spatial sampling (and their footprint sizes) on uncertainties corresponding to a) product
129 intercomparisons at regional scales and b) in-situ validation practices at coastal ocean
130 sites (local scales). In order to isolate the uncertainties to a sensor's spatial sampling, we
131 follow a simulation approach. Our focus is to model Terra MODIS (MODIST), Aqua
132 MODIS (MODISA), and VIIRS OC products at regional and local scales using the 30m
133 OC products derived from the Operational Land Imager (OLI) onboard Landsat-8 (Irons
134 et al. 2012). To assess the impact of spatial sampling on satellite product
135 intercomparisons, the simulations are performed on a daily basis for 30 (globally
136 distributed) OLI scenes for a 16-day orbital repeat cycle of Aqua, Terra, and SNPP. Then,
137 simulated MODISA products are independently compared against a) simulated VIIRS
138 and b) simulated MODIST products. To simulate the impact on in-situ
139 calibration/validation efforts, the OC products (MODISA, MODIST, and VIIRS) are
140 simulated with more than 100 OLI scenes over eight different known in-situ stations

141 (covering various environmental conditions) for a similar orbit cycle as above. The OLI
142 observations surrounding the stations represent the "truth" and are employed to examine
143 the matchup quality against the simulated coarse resolution OC products. With this
144 approach, the OLI-derived OC products and their spectral contents form the basis of the
145 simulations.

146 The following section (Section 2) elaborates on the necessary steps pursued to
147 simulate OC products from relatively fine-resolution OLI products. Section 3 contains
148 results associated with uncertainties in product intercomparisons and in-situ validations,
149 which is followed by the discussions in Section 4. In the conclusion section, we make
150 recommendations for improving uncertainty assessment of OC products and provide
151 guidelines for future developments.

152 **2. METHODS**

153 The VIIRS instrument aboard SNPP was launched in 2011 to pursue the heritage
154 global measurements made by MODIS on Aqua and Terra. Although VIIRS shares
155 similar operational and climate science requirements with MODIS, it has notable
156 differences in design, calibration, and onboard processing (Baker 2011; Cao et al. 2013).
157 MODIS is a rotating mirror, which sweeps one scan across track while projecting it onto
158 10 square detectors (1km ocean bands). In contrast, VIIRS is a rotating telescope with a
159 half-angle mirror, which projects one sweep of scan onto 16 rectangular detectors, i.e.,
160 750*m* Moderate (M)-bands. The Aqua and SNPP missions are both in ascending orbits
161 crossing the equator around 13:30 local time, while Terra (similar to Landsat-8) is in a
162 morning orbit with nominal 10:30 equatorial crossing time.

163 The projected area of a detector (square or a rectangle) on the ground represents an
164 ideal spatial sample. However, the extent within which an instrument views (and
165 samples) a spot on the ground is commonly larger than the projected detector area due to
166 imperfect optics, jitter, electronics, and post-processing (Holst 2008; Schott 2007). The
167 spatial sampling function is recognized as the point spread function (PSF). The overall
168 PSF of an imaging system is the convolution of the above-noted, component-specific
169 PSFs. The overall spatial performance is specified by the PSF(x, y), which is the product
170 of the measured line spread functions along-track (y) and along-scan (x). For a pair of
171 MODISA-VIIRS or MODIST-MODISA daily observations/products, each instrument
172 views a target of interest from a different vantage point, which yields varying projected
173 sampling area, i.e., the ground sample distance (GSD). The GSD is commonly defined at
174 the Full-Width-Half-Maximum (FWHM) of the PSF (Schott 2007). The size and the
175 shape of a footprint (one spatial sample) of an optical imager is a function of the orbit, the
176 viewing geometry (line-of-sight), and the instrument effective spatial performance. The
177 spatial performance is commonly characterized prior to launch (Lin et al. 2013) and is
178 monitored commonly in the frequency domain throughout the mission either through
179 onboard measurements (Xiong et al. 2006) or through observations of reference targets
180 (moon, uniform edges, etc.) (Xiong et al. 2004).
181 When comparing two OC products at the swath level, the differences due to spatial
182 sampling largely depend on the spatial heterogeneity of the site, i.e., pixel/scene content.
183 Similarly, the fidelity of an in-situ matchup is highly affected by the spatial uniformity
184 around the site. In the following, we describe the simulation procedure implemented for
185 different OLI scenes representing distinct coastal water conditions to obtain reliable

186 statistics on the extent of the impact of spatial sampling on coastal OC products. A
187 thorough description of the procedure is first given for the regional product
188 intercomparisons followed by a short explanation of the simulations implemented at in-
189 situ sites.

190 **2.1. Regional Simulations**

191 **2.1.1. Retrieval of Rrs Products from OLI**

192 The OLI onboard Landsat 8 has been shown to considerably outperform previous
193 generation of Landsat sensors when studying aquatic systems (Gerace et al. 2013;
194 Pahlevan and Schott 2013). This is because of its improved SNR, the 12-bit radiometric
195 resolution, and the addition of the new 443-nm channel (Pahlevan et al. 2014;
196 Vanhellemont and Ruddick 2014). The OLI Level-1 data products (TOA reflectance)
197 were obtained from the USGS web portal (http://glovis.usgs.gov/). In order to provide
198 30m OC products, the OLI data were processed using the SeaDAS package (Franz et al.
199 2015). The calibration gains obtained via cross-calibration at the top-of-atmosphere
200 (TOA) reflectance domain were applied to the original OLI observations (Pahlevan et al.
201 2014). However, it should be emphasized that the absolute product accuracy of the OLI
202 products are not critical in our study. What is important is to obtain relative in-water
203 spatial features present in various environmental conditions. Owing to the non-zero
204 reflectance in the near-infrared (NIR) portion of the spectrum, we used two different
205 atmospheric corrections (ACO) and chose the OLI products with more valid and
206 smoother products based on analyzing the standard deviations for all valid pixels. The
207 ACO was implemented using a) the combination of the two short-wave infrared (SWIR)
208 bands (Vanhellemont and Ruddick 2015) and b) the combination of NIR-SWIR (865nm-
209 2201nm) with the iterations on the NIR channel to account for non-zero reflectance

(Bailey et al. 2010). In these techniques, the aerosol model selection is carried out using Rayleigh-corrected SWIR or NIR-SWIR reflectances. Prior to the aerosol-model selection, the input Rayleigh-corrected reflectances (within the NIR and SWIR channels) were smoothed using a 5×5 averaging filter to increase effective SNR (Gerace et al. 2013). For the product intercomparison, 25 OLI cloud-free scenes (globally distributed as shown in Fig. 1) were processed. The preliminary products over high-latitude areas and turbid atmospheric conditions showed noisy R_{rs} retrievals. This is attributed to the noisy nature of the Rayleigh-corrected reflectances (even after filtering) leading to error in aerosol model selection (Franz et al. 2015). Therefore, the OLI-derived R_{rs} products were further passed through a 3×3 median filter to remove residual noise. This, however, reduces the inherent resolution of OLI data. At this point, the OLI-derived R_{rs} products are supplied to the simulation process as described below. The retrieval of secondary products, including chlorophyll-a ([Chla],(O'Reilly et al. 1998)), diffuse attenuation of downwelling irradiance at 490nm (K_d(490),(Mueller 2000)), and particulate backscattering at 655nm (b_{bp}(655), (Lee et al. 2012)) will be derived (Section 2.1.3) from the simulated coarse-resolution R_{rs} products (Lee et al. 2012).

2.1.2. Implementation

To simulate MODIS (MODIST and MODISA) and VIIRS R_{rs} products using OLI-derived R_{rs} products, the spatial sampling function (PSF) and the (per-observation) line-of-sight information of the sensors are needed.

2.1.2.1. PSF Modeling

231 As described, the PSF is essentially a 2D distribution function that weighs the
232 incoming surface-reflected (or emitted) radiance. For the purpose of this study, the Line
233 Spread Functions (LSFs) measured during the pre-launch characterization of MODIS and
234 VIIRS were employed (Barnes et al. 1998; Lin et al. 2013). Note that, due to inherent

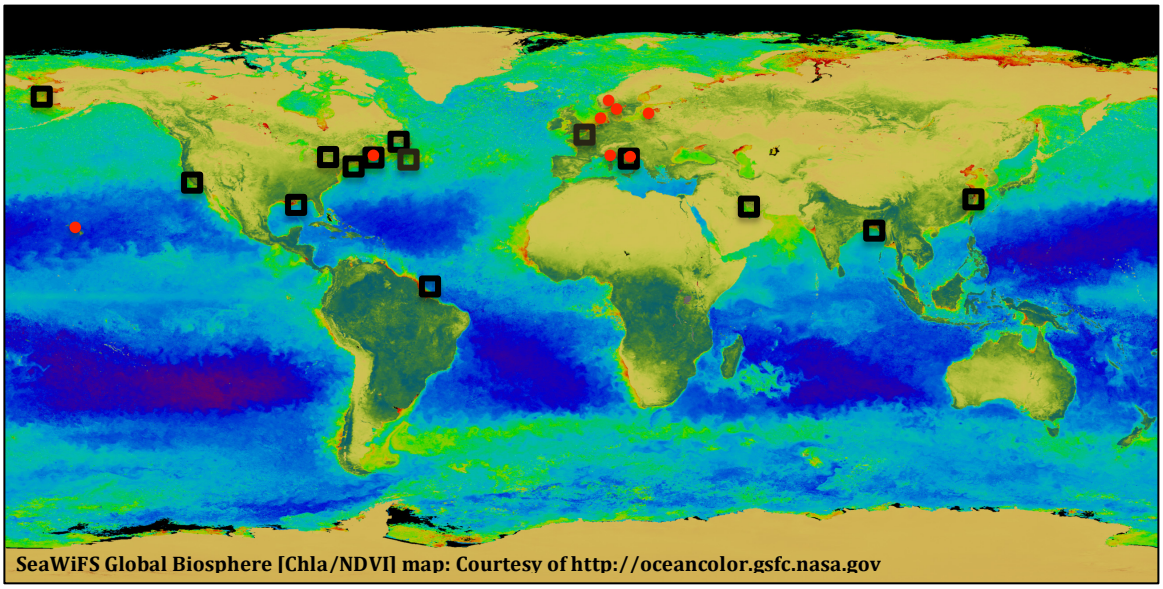

Fig. 1. The sites (indicated by boxes) where OLI scenes are processed to Level-2 OC products for intercomparisons of products at regional scales (Section 2.1). For these locations, the MODISA, MODIST, and VIIRS OC products were simulated according to their corresponding viewing geometries from DOY=1 to DOY=16 in 2015. The red dots denote the locations where simulated matchups were produced and analyzed (Section 2.2).

235

236

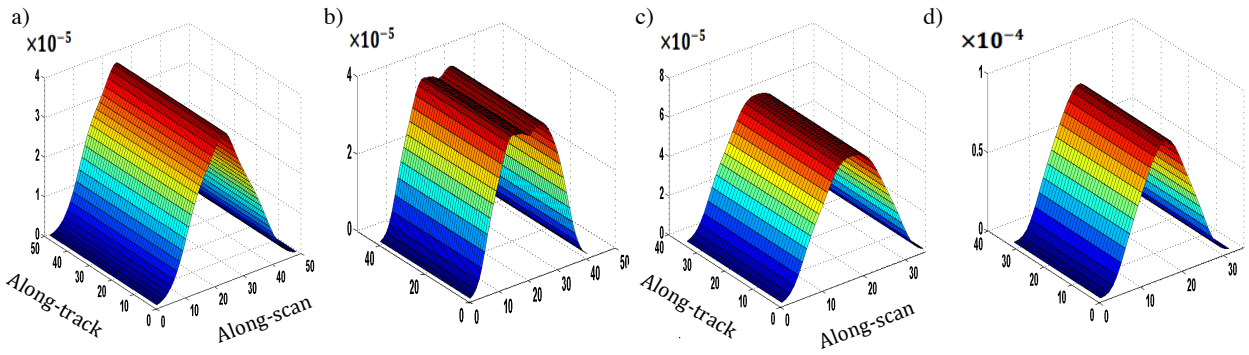

Fig. 2. The band/detector average point spread functions (PSFs) shown for a) MODIS, b) VIIRS near-nadir zone (PSF-V3g), c) VIIRS mid-range zone (PSF-V2g), and d) VIIRS edge-of-scan zone (PSF-V1g). Note that it is assumed that the along-track response is rectangular (ideal response). All the functions have unit-area. The coordinates are in arbitrary pixel units.

237 similarities in shape, only one set of LSF was utilized for MODISA and MODIST. The
238 LSFs had been characterized for each detector in each band. In general, the MODIS
239 along-scan LSFs, i.e., LSF(x), can be approximated as triangular functions (Wolfe et al.
240 1998).
241 For VIIRS, however, the onboard aggregation yields different along-scan LSFs for each
242 aggregation zone (Cao et al. 2014). VIIRS has been designed with rectangular detectors
243 (with the smaller dimension along-scan) to allow for aggregating (averaging) multiple
244 samples. At near nadir scan angles ($\alpha < 31.72°$) every three pixels are aggregated, in
245 mid-range angles ($31.72° < \alpha < 44.86°$) every two pixels are aggregated, and at the
246 edge of the scan ($\alpha > 44.86°$) no averaging is implemented. This scheme provides near-
247 uniform sampling of the Earth surface in the along-scan (x) direction and reduces the
248 "pixel growth" at the edge of the scan to less than 2.2× the linear dimension of the nadir
249 pixels (Fig. 8 in Cao et al. (2014)). The MODIS along-scan samples at the edge of the
250 scan, however, are nearly five times larger than those at nadir. On the other hand, at the
251 edge of the scan, the size of the MODIS and VIIRS along-track footprints are very
252 similar, i.e., ~ twice larger than the footprint sizes at nadir-viewing angles (Wolfe et al.
253 2013). For an accurate simulation of the effects of spatial sampling on OC products, the
254 four different LSF(x) (Fig. 2) are modeled to represent the spatial sampling of MODIS
255 and VIIRS. The along-scan LSFs, as a result, are modeled as the summation of multiple
256 Gaussian functions, which provided the best fit to the measured LSFs:
257
258 $$LSF(x) = \sum_{i=1}^{5} a_i \, exp\left(\frac{x-b_i}{c_i}\right) \quad (1)$$

where b and c are the mean and the standard deviation for each Gaussian function, respectively, and $i = 1, \ldots, 5$ represents indices attributed to the Gaussian functions. The $\mathrm{PSF}(x, y)$ is a separable function and can be constructed by assuming a rectangular LSF along-track (y) as below (Lin et al. 2013):

$$\mathrm{PSF}(x, y) = \mathrm{LSF}(x) \times \mathrm{LSF}(y) \quad (2)$$

where $\mathrm{LSF}(x)$ and $\mathrm{LSF}(y)$ are the along-scan and along-track spatial responses of MODIS and VIIRS, respectively. Fig. 2 shows the unit-area PSFs employed to simulate MODIS and VIIRS scenes. Note that the discrepancies amongst band- or detector-dependent LSFs are assumed negligible and average sampling functions of 1000m ocean bands (MODIS) and 750m M-bands (VIIRS) are used. Also, in this study, the optical scattering (leakage) outside of the instantaneous field-of-view of a detector has been ignored (Meister and McClain 2010). The PSFs constructed using Eq.2 are further scaled and rotated per observation (pixel) according to the line-of-sight geometries.

2.1.2.2. Line-of-sight Geometry

In addition to the PSF modeling, the corresponding line-of-sight information is extracted from the geolocation products. The MODIS geolocation products (MYD03 and MOD03 corresponding to MODISA and MODIST, respectively) were obtained from the NASA's Level-1 and Atmosphere Archive and Distribution System (LAADS) while those of VIIRS (GMODO) were downloaded from the NOAA's Comprehensive Large Array-data Stewardship System (CLASS). The geolocation products allow for reconstructing per-pixel (-observation) line-of-sight geometries. The line-of-sight

information includes per-pixel geographic latitude and longitude, the view zenith angle (VZA), the view azimuth angle (VAA) relative to the North, and the satellite range (R), which is defined as the distance between the sensor and ground (Baker 2011). While the standard MODIS geolocation products are available at 1km grid resolution, the inherent VIIRS geolocation grids are at 750m.

The 30m OLI R_{rs} products are sampled with MODIS and VIIRS PSFs and their respective line-of-sight geometries on a daily basis (for 16 days). The supports of the PSFs (Fig. 2) are essentially scaled and rotated in along-track and along-scan directions given per-pixel VZA, VAA, and R (Schowengerdt 1997). The PSFs are convolved with OLI R_{rs} products in a discrete form as follows:

$$S_n^k = \sum_m \sum_i \sum_j PSF_{(VZA_m, VAA_m)}(i,j) * R_{rs}^k(i,j) \quad (3)$$

where S_n^k is the simulated VIIRS or MODIS sub-granule swath for the *n*th day $(1 < n < 16)$, k is the channel number, $R_{rs}^k(i,j)$ indicates the remote sensing reflectance attributed to a pixel location (i,j) on the OLI grid for band k, and $PSF_{(VZA_m, VAA_m)}$ is the PSF implemented for a given VZA_m and VAA_m, where m is an observation (pixel) index associated with MODIS or VIIRS geolocation products (Wolfe et al. 2002). The four OLI visible channels (i.e., $k = 1, 2\ 3, 4$ which represent 443, 482, 562, and 655nm) are processed during the simulation (Pahlevan and Schott 2013).

The MODIS footprint size was computed using range, VZA, and MODIS effective focal length (380mm) for the along-scan and along-track directions(Schowengerdt 1997). On the other hand, due to the onboard aggregation scheme of VIIRS, there is no such a

direct relationship between VZA and footprint size. Therefore, the footprint size of VIIRS in along-scan and along-track was calculated by quadratic modeling of the scan-angle-versus-foot-print size relationship (Cao et al. 2014). This was done by specifying observational aggregation zone (for VIIRS) and recalculating the scan angle from a given VZA as below

$$\alpha = sin^{-1}(sin(180 - VZA)\, R_e/(R_e + H)) \quad (4)$$

where R_e is the Earth radius for a given latitude and H stands for the VIIRS orbit altitude at nadir. To provide concrete examples, the along-scan size of a MODIS and VIIRS observation cell at nadir is approximately 2200m and 1160m, respectively, which are nearly 2.2 and 1.5 times larger than the projected size of the detectors on the ground (e.g., ~ 750m for VIIRS). With this approach, simulated VIIRS or MODIS granules (5-min MODIS granules in case of MODIS) are created. Since only the OLI effective area is filled with valid R_{rs} values in the granules, we refer to the resulting swath as sub-granules. Fig. 3 shows an example of an OLI scene and the simulated MODISA, MODIST, and VIIRS. In this example, an OLI-derived chlorophyll-a product is "scanned" given MODISA, MODIST, and VIIRS viewing geometries. Note the differences in the average VZAs for the three simulated ocean color scenes.

2.1.2.3. Time Period

While the OLI R_{rs} products come from various coastal systems during different times/seasons (see Appendix), simulations of MODIS and VIIRS granules are performed

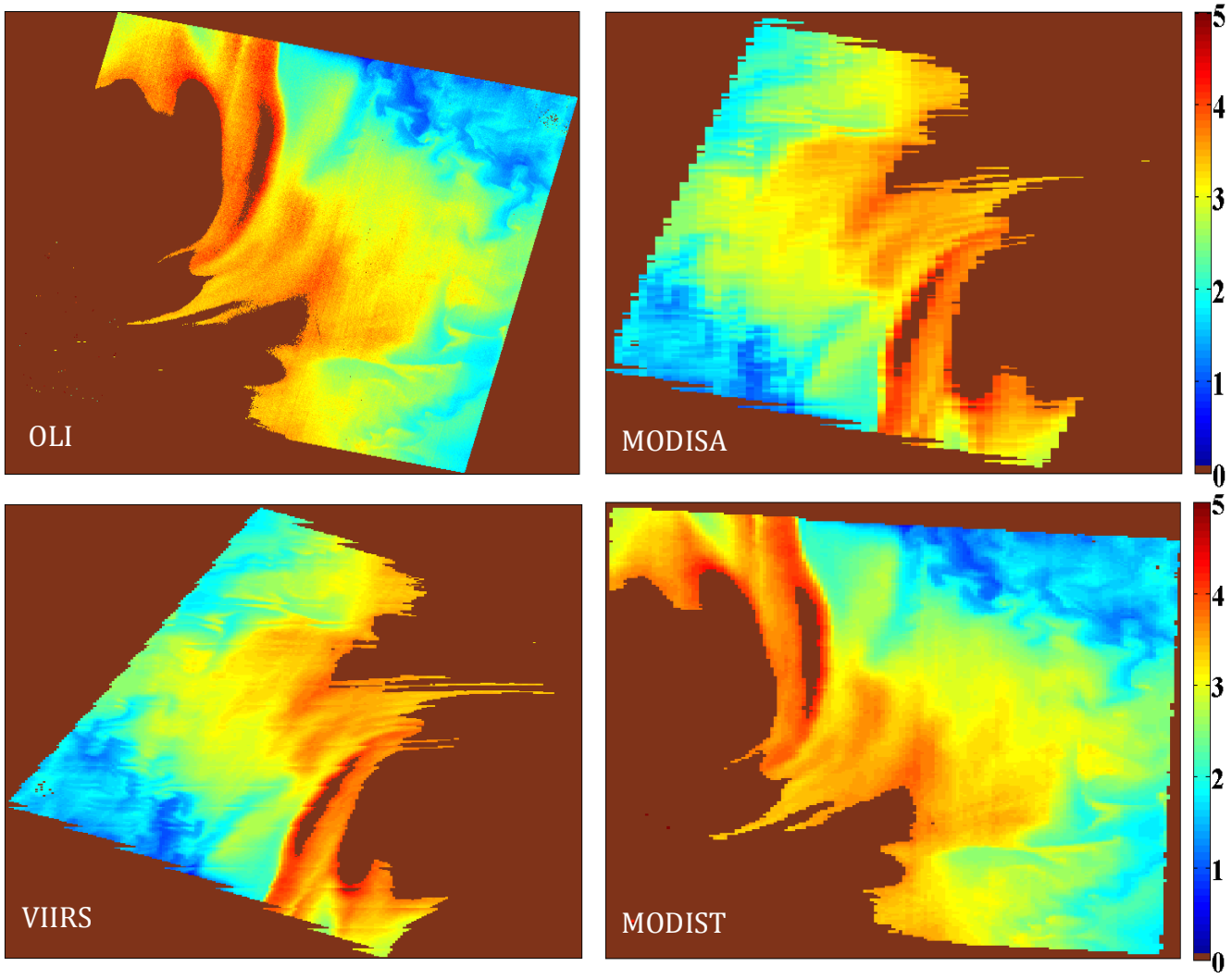

Fig. 3. Examples of simulated MODISA, VIIRS, and MODIST swaths for [Chla] ($\boldsymbol{mg/m^3}$) fields derived from the OLI-derived [Chla] products over the Yangtze River mouth, East coast of China. The average view zenith angles (VZAs) are 58.18°, 51.5°, and 21.5° for MODISA, VIIRS, and MODIST swaths, respectively. The features are reproduced at different viewing conditions. Note that OLI and MODIST are in descending orbits. Also, the extremely turbid waters over the basin are masked.

for an arbitrary orbital repeat cycle of Aqua/Terra/SNPP starting from January 1st (DOY=1) to January 16th (DOY=16) in 2015. This is to maintain the orbit geometries similar for all the simulations, which allows for consistent product intercomparisons across all simulated products. Note that only viewing geometries of ocean color sensors are extracted over this period of time and the OLI scenes correspond to different days of year and environmental conditions. It should be noted that daily intercomparisons are carried out only for days that both granules fully cover an OLI scene across track. This is to ensure that there is a one-to-one comparison between simulated MODIS and VIIRS R_{rs} products. Note that for higher latitude OLI scenes (e.g., Alaska scenes), there are more than 16 pairs of MODISA-VIIRS (or MODIST-MODISA) intercomparisons.

2.1.3. Retrieval of Secondary OC Products

After MODISA, MODIST, and VIIRS R_{rs} swath-level products are simulated, [Chla], $K_d(490)$, and $b_{bp}(655)$ are computed using standard algorithms available in SeaDAS (http://seadas.gsfc.nasa.gov). For [Chla], we used the OC3 algorithm (O'Reilly et al. 1998; O'Reilly et al. 2000), which was recently adapted for the spectral bands of OLI (Franz et al. 2015). Similarly, for $K_d(490)$ we used the KD2 algorithm (Mueller 2000) with the OLI-specific tuning provided in SeaDAS. And finally, for $b_{bp}(655)$ we used the QAA inherent optical properties algorithm of Lee et al. (2002). It should be further emphasized that the absolute accuracy of retrievals are not critical in our study. What is important is capturing varying coastal-ocean spatial features (swirls, river plumes, eddies, etc.) of different sizes through OLI observations and the derived products.

2.1.4. Gridding

356 The swath-level R_{rs} products are commonly distorted geographically (Fig. 3)
357 rendering it impossible to make pixel-to-pixel comparison. For a particular day of Terra
358 and Aqua's overpasses (e.g., DOY=4), consider arbitrary MODISA and MODIST
359 observations, which view an OLI scene at two significantly different viewing angles. The
360 per-observation inter-comparisons of the two swaths are hindered by significantly
361 different levels of distortions for the pair of observation (e.g., ~6km MODISA pixels
362 against ~1km MODIST pixels). For this reason, the simulated sub-granules (S_n^k) are
363 gridded to 1km sinusoidal grid cells (S_n^{kG}) (Wolfe et al. 1998) using the nearest-neighbor
364 technique (Campbell et al. 1996). The 1km grid was chosen to closely match the near-
365 nadir nominal resolution of MODIS and VIIRS over spatially variable coastal waters.
366 The gridding allows for a uniform cell-by-cell comparison.

367 **2.2. Local Simulations**

368 With the simulation routine in place, it is also possible to provide insights into how
369 well a discrete in-situ sample taken during a field campaign or at a field station represents
370 an observation made by MODISA, MODIST, or VIIRS (Mélin et al. 2007; Moore et al.
371 2015). To do so, OLI pixels were used to represent a sample measurement in the field or
372 at a site. These locations can well be arbitrary, however, it was decided to carry out this
373 analysis at known field sites where routine radiometric observations are made for OC
374 calibration/validation purposes. We chose AERONET-OC stations (Zibordi et al. 2009b)
375 located near Venice (Venise), Martha's Vineyard (MVCO), Gustav Dalén (Gustav),
376 Helsinki Light House (Helsinki), Zeebrugge, and Palgrunden (Fig. 1) to represent
377 spatially variable waters at the proximity of coastal waters (http://aeronet.gsfc.nasa.gov).
378 We further used the locations at the Marine Optical Buoy (MOBY) (Clark et al. 1997)
379 and the BOUSSOLE site (Antoine et al. 2008b) to assess spatial variability in clear

380 waters. The latter two sites are buoys where in-situ radiometric observations are made to
381 calibrate TOA OC observations. It is stressed that we do not incorporate the actual
382 radiometric measurements at these sites. All the available cloud-/glint-free OLI scenes
383 over the selected sites (totaling 120) were obtained from the USGS database. Similar to
384 the previous section, the field sites were observed (scanned) for one orbit cycle (DOY=1
385 through DOY=16) of Aqua, Terra, and SNPP. Therefore, the 16-day simulated products
386 (locally) are computed for each OLI sample scene (Section 2.1.2.3).

387 For processing the OLI TOA products, although best-practice atmospheric correction
388 was employed (similar to Section 2.1.1; a combination of NIR-SWIR), there remains a
389 small percentage of OLI pixels flagged for poor quality (due to ship wakes, significant
390 resuspension events, etc.). Like the previous section, the OLI-derived OC products were
391 processed with a 3×3 median filter prior to implementing the simulations (Section 2.1.2).
392 The simulation was performed for one pixel, i.e., 1×1 window, as well as a 3×3 window,
393 and a 5×5 window of MODISA, MODIST, and VIIRS pixels surrounding the site
394 location to scrutinize in-water spatial variability at observation scales. Following multiple
395 experiments, it was decided to discard simulation results (OC pixels) for which more than
396 5% of the OLI pixels (falling under one ocean color footprint) are flagged. The major
397 reasons for pixel-flagging in case of our cloud-free OLI scenes were failure of the
398 atmospheric correction and the presence of land boundaries or marine vessels). When this
399 criterion is passed, the remaining flagged pixels (< 5% of total) are ignored and not
400 included in further statistical analysis. Moreover, the simulation ocean color footprints
401 were discarded if CV calculated for a window exceeded a threshold of 0.15 (Bailey and
402 Werdell 2006). To further minimize impacts of OLI residual scene noise (i.e., striping),

the same criterion was tested for the OLI pixels falling under the window under investigation. To simulate the in-situ radiometric observation at the site, a window of size 5×5 (centered at the site location) was used to extract OLI-derived pixels totaling 16. This is to , exclude the center 3×3 elements to avoid adjacency effects (Storey et al. 2014). The median value computed from the 16 pixels was found to best represent the measurement at the site. To emulate calibration/validation activities at these sites, the gridding scheme (Section 2.1.4) was excluded in this section. Therefore, comparisons were made at swath-level observations.

2.3. Metrics

To gauge how two sets of products (derived from sensors A and B) compare, multiple metrics are defined. The per-cell (*i*) percent difference is defined as:

$$RPD^i = \left(R_A^i - R_B^i\right) / \left[\left(R_A^i + R_B^i\right)/2\right] \quad [\times 100] \tag{5}$$

where R_A^i and R_B^i stand for per-grid cell (*i*) simulated products for products derived from sensors A and B. In a slightly different manner, the absolute relative percent difference can be calculated

$$ARPD^i = \left|R_A^i - R_B^i\right| / \left[\left(R_A^i + R_B^i\right)/2\right] \quad [\times 100] \tag{6}$$

The median and mean values of RPD and ARPD over an entire grid can be used to specify the overall discrepancies for a product pair (Table 1). To further get insights into the differences in an absolute sense (product units), we also provide the root-mean-squared difference for *N* grid cells computed as below

$$RMSD = \sqrt{\frac{\sum_{i=1}^{N}\left(R_A^i - R_B^i\right)^2}{N}} \tag{7}$$

Also, histograms of the RPD sub-granules (Eq. 5) provide valuable statistics on a per-grid cell basis. Based on a histogram, multiple discrepancy metrics can be defined. In particular, we use the 1st momentum of the histogram to refer to the mean bias. We also define the Percent of Pixels (PoP) within the $\pm z\%$ range of the histogram mean. The PoP (%) is a metric that specifies the percentage of pixels that fall within the $\pm z\%$ of the mean of the histogram. For instance, when $z = 1\%$, the percentage of grid cells exhibiting differences less than 1%, i.e., $-1\% < RPD^i < +1\%$, is expressed. This is represented by PoP @ $z = \pm 1\%$. Fig. 4 illustrates a sample RPD histogram computed from simulated VIIRS and MODISA sub-granule R_{rs} products with z ranging within $\pm 10\%$. For a given pair of simulated gridded products, the narrower the histogram the more homogenous the site is. To eliminate outliers from our analysis, we restrict RPD within the $\pm 60\%$ range. These outliers commonly occur at land-water interfaces, where

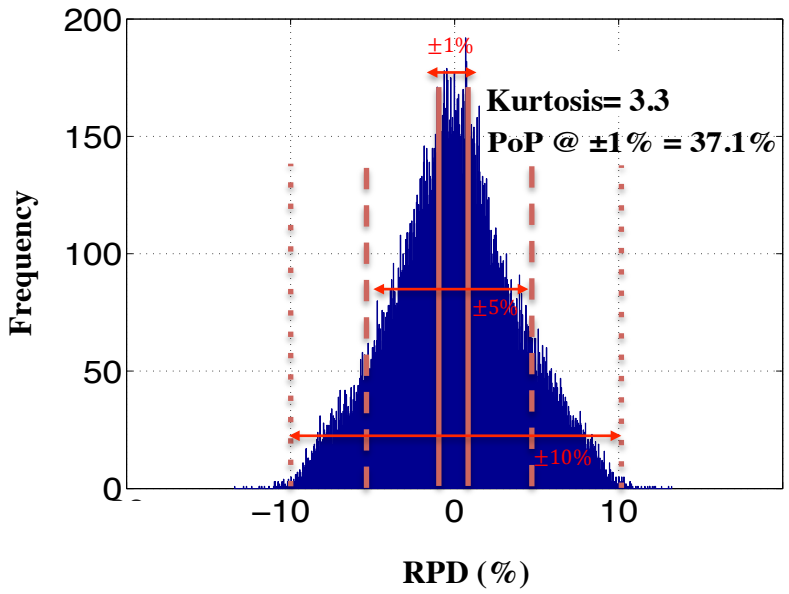

Fig. 4. A typical histogram derived from product intercomparisons. Amongst different histogram-derived parameters, the Percent of Pixels (PoP) is shown above for various levels of relative percentage difference, i.e., RPD= 1%, 5%, and 10%. Also, histogram kurtosis indicates how spread is the distribution around the histogram mean. The narrower the histogram, the more consistent a pair of products are.

discrepancies in the footprint sizes result in seemingly large differences. The other histogram-derived metric is kurtosis (K). Kurtosis is the fourth moment of the distributions, which is a descriptor of the shape of the distribution and explains how narrow a distribution is relative to that of a normal. For a normal distribution, the kurtosis value is ~3. The narrower the shape of a histogram, the larger the kurtosis value is. For example, when $K = 10$, a product pair is found more consistent than if K were equal to 3. The overall analysis of these metrics helps understand how the combination of imaging geometry and spatial sampling contribute to the differences in ocean color products at regional scales.

For the OC simulations over field stations, we used a slightly different metric termed the percent difference (PD) for the station (*s*) as below

$$PD^s = (R_X^s - R_{OLI}^s)/R_{OLI}^s \quad [\times 100] \tag{8}$$

where R_X^s represents the median (within a 3×3 or 5×5 box) simulated observations (for the sensor *X*) and R_{OLI}^s is the median OLI OC products within a 5×5 box centered over the field station *s*. Note that we excluded the 3×3 pixels at the center, which effectively allowed 16 pixels for calculating the median value. The PD can be utilized to obtain an estimate of the temporal mean bias at a field station (e.g., MOBY). The absolute percentage difference can also be used to provide further insights into matchup analysis:

$$APD^s = |R_X^s - R_{OLI}^s|/R_{OLI}^s \quad [\times 100] \tag{9}$$

The metric APD is used to explain how close a simulated in-situ R_{rs} is to that derived from satellite observations. Note that for simulating matchups, we only evaluate differences in R_{rs}.

3. RESULTS

The uncertainties induced by spatial sampling are presented for two data quality assessment approaches: a) intercomparisons of products derived from two different OC sensors and b) products compared against "in-situ measurements" at eight different sites. While the former provides insights into the discrepancies in products at regional scales (Landsat scene size; $185km \times 185km$), the latter is an assessment of spatial representativeness at the selected field sites.

3.1. Regional Assessment

3.1.1. Product Consistency

In this section, the kurtosis value is used to describe the overall discrepancies between product pairs. Fig. 5 illustrates the kurtosis values (K) as a function of differences in the mean view zenith angles ($\overline{VZA}$) for the three selected sites. The mean view zenith angle is computed by taking the average of VZAs with which the OC sensor "views" (scans) an OLI scene. The differences in $\overline{VZA}$, i.e., $\Delta VZA = \overline{VZA}_V - \overline{VZA}_{MA}$ and $\Delta VZA = \overline{VZA}_{MT} - \overline{VZA}_{MA}$, are binned into 10° intervals. The subscripts MA, MT, and V correspond to MODISA, MODIST, and VIIRS, respectively. For each OLI scene, at least 12 pairs of simulations for MODISA-VIIRS and MODIST-MODISA are incorporated. The error bars denote one-standard deviation for the data points (associated with mean K) situated within a ΔVZA bin. The differences in angles (ΔVZA) range from -60° to $+60^{\circ}$ on the x-axes. Figs. 5a-c correspond to VIIRS-MODISA intercomparisons of R_{rs}, [Chla], $K_d(482)$, and $b_{bp}(655)$ products. It is clearly seen that the interconsistency between all products improves towards positive ΔVZAs, i.e., narrower histograms on the right side of the plots. On average, the products are more consistent by a factor of two when the edge-of-the-scan VIIRS products are compared against near-nadir products of MODISA.

494 This is attributed to larger along-scan footprint sizes of VIIRS at the edge of the scan
495 (~ 2.7km) against the 2.2km along-scan MODISA footprint sizes at nadir-viewing
496 geometries. On the other hand, the discrepancies between MODIST and MODISA
497
498

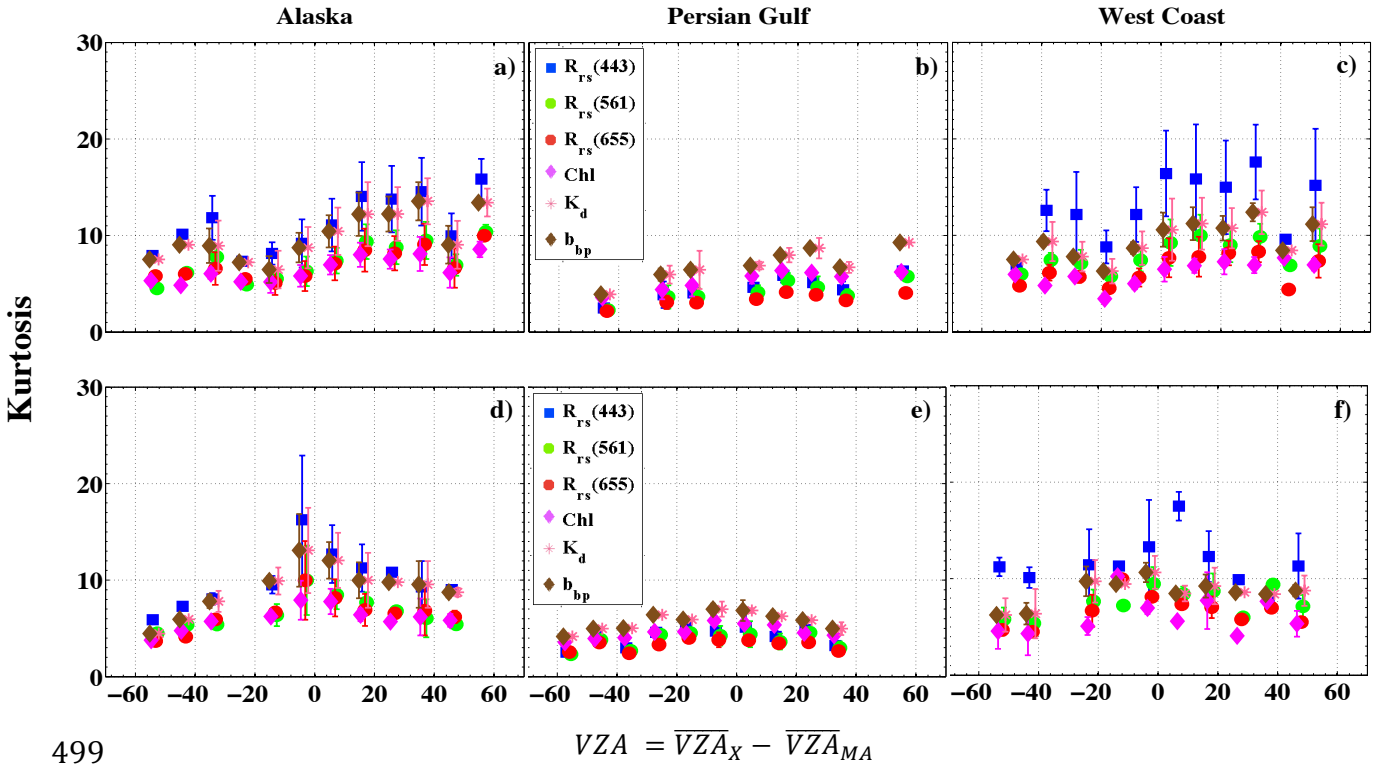

499

Fig. 5. The kurtosis values (derived from the RPD histograms) are shown as a function of differences in mean VZAs ($\overline{\boldsymbol{VZA}}$). The subscript *X* denotes VIIRS (V) or MODIST (MT). The top row shows the asymmetric trends when MODISA and VIIRS products are compared. The x-axes denote $\Delta\boldsymbol{VZA} = \overline{\boldsymbol{VZA}}_{\boldsymbol{V}} - \overline{\boldsymbol{VZA}}_{\boldsymbol{MA}}$. This trend implies that the products are more consistent when $\overline{\boldsymbol{VZA}}_{\boldsymbol{V}} > \overline{\boldsymbol{VZA}}_{\boldsymbol{MA}}$, which yield similar footprint sizes for the two observations. The bottom row corresponds to the intercomparisons of MODISA and MODIST products as a function of $\Delta\boldsymbol{VZA} = \overline{\boldsymbol{VZA}}_{\boldsymbol{MT}} - \overline{\boldsymbol{VZA}}_{\boldsymbol{MA}}$. Although MODISA and MODIST are in afternoon and morning orbits, , there is no particular trends found when comparing the associated products at different VZAs.

500
501
502
503
504

505 products exhibit symmetric trends around $\Delta VZA = 0$ (Fig. 5d-f). It is, thus, inferred that
506 although Aqua and Terra are in different morning and afternoon orbits, due to their
507 similarities in spatial sampling and footprint size, there are no distinct trends observed on
508 either side of the plots. The K values also provide clues on the in-scene spatial variability
509 at each site. For instance, the K values for the Persian Gulf site are, on average, smaller
510 than those for the Alaska and the Monterey Bay sites (indicating its larger inherent in-
511 water variability). While K values (and also PoP not shown here) show evidence for the
512 angular dependency of product interconsistency at regional scales, the mean RPD (same
513 plots as in Fig. 5 but for mean RPD not shown here for brevity) does not evidently exhibit
514 angular dependency. This implies that the use of representative statistics (e.g., mean RPD
515 and ARPD) computed at regional scales can minimize the overall product inconsistencies
516 (as opposed to pixel-by-pixel comparisons captured by K and PoP). Table 1 contains the
517 overall statistics calculated for all sites. As expected, for all the products compared in this
518 study, the mean RPD values converge to zero validating that overall intercomparisons at
519 regional scales ($185km \times 185km$ in this study) are immune from the effects of
520 differences in spatial sampling. Note that the RPD ranges within the $\pm 60\%$ with
521 histograms resembling the normal distribution, that is, the differences can reach up to
522 60%. The comparisons in the ARPD domain (absolute relative percent differences
523 computed for all scenes) show percent differences falling within the 1% to 4.5% range.
524 This varies depending on whether the mean or median metrics are considered. We refer
525 to the mean ARPD values (averaged for the two sets of intercomparisons), as the
526

Table 1. The overall product intercomparisons statistics, i.e., median (med), mean, and RMSE, averaged and tabulated for all sites.

		$R_{rs}(443)$	$R_{rs}(482)$	$R_{rs}(561)$	$R_{rs}(655)$	[Chla]	$K_d(482)$	$B_{bp}(655)$
VIIRS Vs. MODISA	Med (RPD) [%]	0.0035	0.0029	0.0005	0.0004	-0.0045	-0.0008	-0.0031
	Mean (RPD)[%]	0.0133	0.0049	-0.0060	-0.0291	-0.0100	-0.0014	-0.0164
	Med (ARPD)[%]	0.7802	0.8114	1.0604	1.5287	1.5814	0.9795	1.9116
	Mean (ARPD) [%]	1.5870	1.6899	2.1482	4.0010	2.8950	1.9385	4.2637
	RMSE	0.0004	0.0004	0.0004	0.0002	0.1423	0.0124	0.0022
MODIST Vs. MODISA	Med (RPD) [%]	0.0009	0.0007	-0.0001	-0.0043	-0.0141	-0.0032	0.0000
	Mean (RPD)[%]	-0.0052	-0.0021	-0.0096	-0.0055	-0.0431	-0.0188	-0.0273
	Med (ARPD)[%]	0.8660	0.8848	1.2238	2.2307	1.3995	0.7839	1.4984
	Mean (ARPD) [%]	2.0921	2.0638	2.6193	4.6604	2.6351	1.6529	3.7957
	RMSE	0.0005	0.0005	0.0005	0.0003	0.1351	0.0123	0.0022

intercomparison uncertainty induced by differences in the spatial sampling that one should anticipate for similar practices in coastal waters. The values computed as 1.8%, 1.9%, 2.4%, 4.3%, 2.7%, 1.8%, and 4% for the $R_{rs}(443)$, $R_{rs}(482)$, $R_{rs}(561)$, $R_{rs}(655)$, [Chla], $K_d(482)$, and $b_{bp}(655)$ products, respectively (Table 1). The RMSD values indicate that, overall, the differences in R_{rs} and [Chla] products are $< 0.0005\ sr^{-1}$ and $< 0.15\ mg/m^3$, respectively.

3.1.2. Uncertainty Thresholds

As noted, the histograms of the RPD grids can be used to interpret the inconsistencies between a product pair. Fig. 6 shows how the percentage of pixels (PoP) lying within a threshold ($\pm z\%$) can change. The results are shown for six sample sites. These curves are the mean values derived from all the daily intercomparisons within one MODISA-VIIRS orbit cycle (MODIST-MODISA comparisons are not shown here). Each marker indicates the percentage of pixels falling within a relative percent difference (RPD) shown on the *x*-axes as z. Note that the x-axes are shown from 1 to 10% (recall from Section 3.2 that

545 the RPDs can reach as high as 60%). The y-axis indicates the PoP (%). Taking the graph
546 associated with the Alaska site as an example, when a 1% RPD in products (R_{rs}, [Chla],
547 $K_d(490)$, $b_{bp}(655)$) is adopted as an accepted threshold (i.e., pixels are assumed
548 consistent), there is, on average, only 40-60% of the pixels that meet this threshold. As
549 one accepts higher uncertainty thresholds more pixels fall within the threshold. As it
550 appears from Figs. 6a & 6d, the product discrepancy is dependent on inherent spatial
551 variability of the coastal ecosystems under study. For the sites with less spatial variability
552 (inferred via visual analyses), over 90% of the products are in good agreement, when
553 uncertainty threshold is set at 2%. Since the shape of the histograms resemble normal
554 distributions, it is also possible to express the uncertainties in intercomparisons as
555 probability. These sites include East China and Saint Lawrence. Consider MODISA-
556 VIIRS discrepancy in [Chla] for the East China site (Fig. 6a), it can be inferred that there
557 is a 68% chance for any given pixel to exhibit differences below $\pm$1%. For the Saint
558 Lawrence site, the inconsistency curves quickly reach 100% for all the products at the ~
559 5% threshold. These results (including those not shown here) indicate that there is, on
560 average, 80% chance that product intercomparisons show inherent differences below 8%
561 (due to the combination of in-scene spatial variability and sensors' viewing geometries),
562 a threshold at which the product can be considered consistent. In other words, there is a
563 20% chance that products show more than ~8% discrepancies. Depending on the
564 application, one may choose different thresholds for such intercomparison analyses.
565 Visual inspections of RPD grids verify that high discrepancies occur at the proximity of
566 land-water interfaces, where the two instruments view such high-contrast regions from

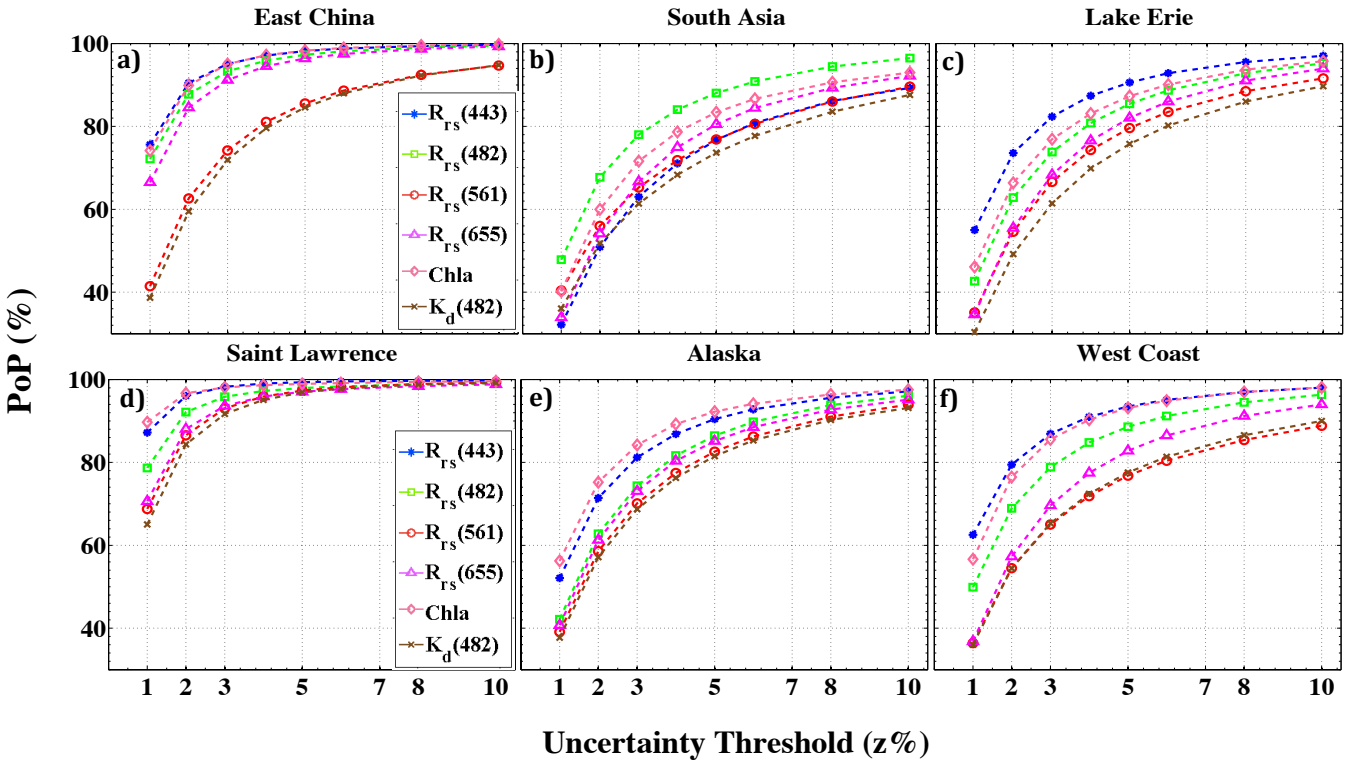

Fig. 6. The spatial interconsistency curves showing the percentage of pixels (PoP) found consistent at different $|\boldsymbol{RPD}|$ thresholds (x-axes). As the absolute RPD increases more pixels (% PoP) are expected to fall within the threshold. On average, more than 80% of the pixels are considered consistent when z=8% difference in products are adopted as the threshold.

577 different vantage points. Note that in actual imaging conditions, adjacency effects
578 may further complicate the discrepancies (Meister and McClain 2010). Although the
579 original OLI products have undergone smoothing and de-noising, there are some signal-
580 dependent trends in the spatial consistency curves (as seen in Fig.6). The red channel and
581 the $b_{bp}(655)$ products (derived from MODISA and VIIRS) commonly show the largest
582 discrepancies, whereas (for sites with $[Chla] < 0.3\, mg/m^3$) R_{rs} (443) product is found to
583 be the most consistent product. This is consistent with the previously published works
584 (Mélin et al. 2007; Moore et al. 2015) and is attributed to the low signal levels
585 measured/retrieved. For all the sites and geometries, K_d (490) is, on average, amongst the
586 relatively consistent products while the [Chla] products exhibit less consistency (slightly
587 better than those of R_{rs} (655) and b_{bp} (655)).
588 The graphs shown in Fig. 6 indicate the interconsistency between products derived
589 from MODISA and VIIRS. It is also important to obtain insights into how VIIRS-
590 MODISA cross-comparisons differ from those for MODIST-MODISA. This would
591 reveal how differences in the orbits and viewing geometries can, overall, contribute to
592 intercomparison in coastal ocean waters. Fig. 7 shows the median ratio of PoPs
593 associated with the MODISA-VIIRS and MODIST-MODISA intercomparisons as a
594 function of varying thresholds (z). It is inferred that the MODISA- and VIIRS-derived
595 products are more consistent (12% at maximum) than MODIST-MODISA products.
596 For instance, there are 8-12% more pixels falling within $\pm 1\%$ threshold (z) when
597 MODISA and VIIRS products are compared, i.e., VIIRS and MODISA are slightly in a
598 better agreement than MODIST and MODISA. This indicates the importance of satellite
599 orbits (ascending versus descending) on product interconsistency and long-term global

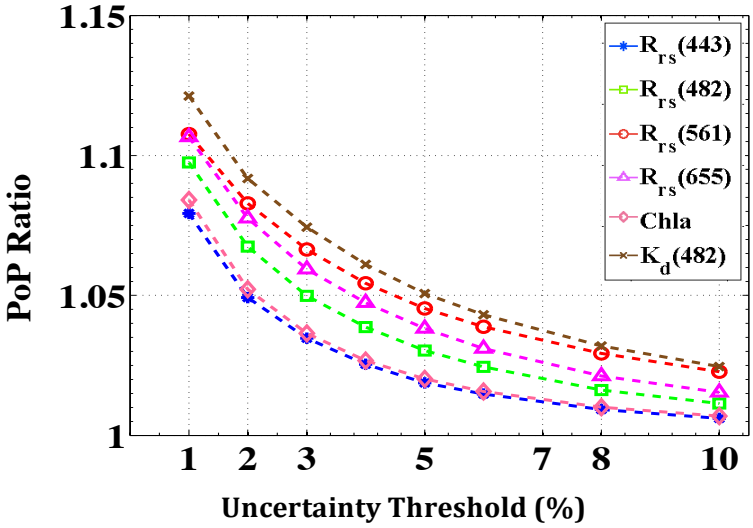

Fig. 7. The ratio of MODISA-VIIRS and MODIST-MODISA intercomparisons (based on PoP) as a function of the uncertainty threshold (absolute RPD). Overall, MODISA and VIIRS products are more consistent than when products of MODIST and MODISA are compared.

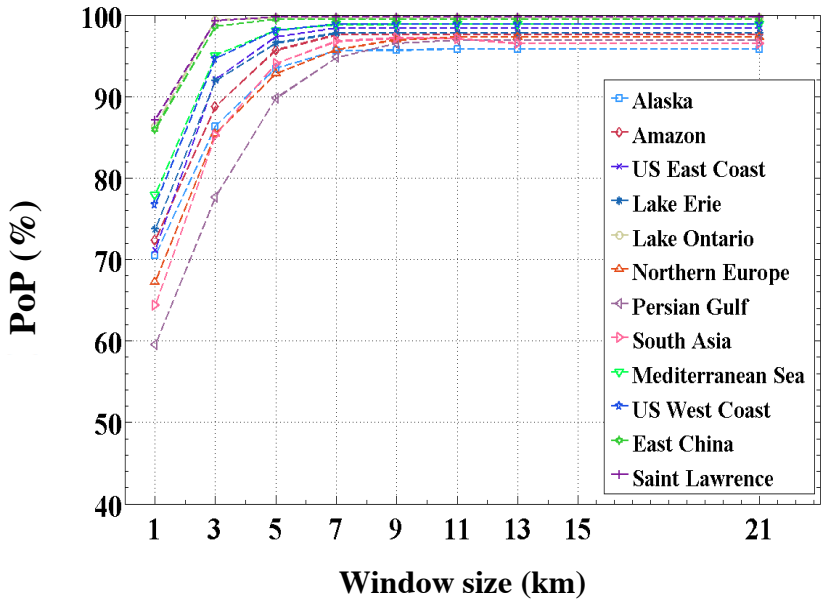

Fig. 8. The spatial consistency curves shown for R_{rs}(443) as a function of scale, i.e., $\boldsymbol{1km \times 1km}$, $\boldsymbol{3km \times 3km}$, etc. The y-axis denotes PoP at z=1%, which increases as the effective grid cell size increases. The optimal scale, on average, is found at 7km.

622 monitoring of coastal oceans. As larger thresholds are adopted, the intercomparisons are
623 expected to become very similar for the two sensor pairs (e.g., less than 3% difference in
624 PoP at $z = \pm 10\%$ threshold). Note that these intercomparisons encompass all
625 observations (pixels) across various OLI scenes, which permits to gauge consistency on a
626 per-grid cell basis between sensor (product) pairs.

627 **3.1.3. Scale-dependency**

628 The intercomparisons presented in the previous section showed product discrepancies
629 at the 1km grid cell size (Section 2.1.4). In this section, we will discuss the spatial scales
630 at which nearly all the pixels meet a $z = \pm 1\%$ difference threshold (RPD). For this
631 purpose, the 1km grid cell is filtered using varying window sizes (i.e., $3\times3, \ldots, 21\times21$).
632 The products (smoothed at different scales) are then compared (i.e., calculating RPD) to
633 quantify at what scale, i.e., window size, they can be regarded as consistent, i.e., the
634 inconsistencies reach a minimum. At such scales, the product intercomparisons can be
635 considered insensitive to the effects of spatial sampling. To exclude the artifacts due to
636 the averaging at the land-water interfaces, the grid cells 21km from these boundaries
637 were not incorporated in the analysis. Fig. 8 illustrates the spatial interconsistency curves
638 for the Rrs(443) products shown for the different sites studied here. The y-axis is the PoP
639 (%) specified for $z = \pm 1\%$ threshold and the x-axis denotes the window size used to
640 smooth the products. As expected the product inconsistencies are at minimum when
641 comparing relatively uniform coastal scenes. This is noticeable for the Saint Lawrence
642 and East China sites, for which the curves quickly peaks when products are smoothed
643 with 3×3 windows, i.e., effective grid size of $3km \times 3km$. However, for most sites, the
644 spatial interconsistency curves plateau (does not necessarily reach 100%) when the

effective grid cell size is $\sim 7km$. This indicates that for relatively reliable product intercomparisons in offshore regions, one may need to perform a low-pass filtering with window sizes of at least 7×7 to *minimize* the impact of high-frequency variations in coastal ocean waters. In our case studies, the exception is the Persian Gulf site where the corresponding curve does not reach a maximum until 9×9 windows are implemented. It is, therefore, surmised that the intercomparison studies at $9km \times 9km$ standard Level-3 products are expected to be least impacted by the effects of spatial sampling, i.e., differences in the viewing geometries, orbits, footprint sizes, etc.). Note that depending on the inherent spatial variability of the sites, there may be some residual differences in the products as seen in Fig. 8 for spatial scales larger than 9km. It is stressed that the result in this section applies to the offshore regions (> 21km off the coastlines), where RPD values, in general, remain below 10% ($|z| < 10\%$).

3.2. Spatial representativeness at In-situ sites

As described in Section 2.2, for the local spatial analysis, the OLI observations at the proximity of the field sites are regarded as the "sea-truth" and compared against simulated coarse OC products. Fig. 9 shows PDs for the available OLI-derived $R_{rs}(443)$ products at the MVCO, Venise, and Zeebrugge sites. Note that the OLI scenes available from 2013 to 2015 are shown for one annual period and grouped according to the OLI observation dates, i.e., OLI scenes. For these sites, MODISA, MODIST, and VIIRS simulated observations are averaged over 3×3 boxes. Several conclusions can be drawn from the graphs. First, although the CV < 0.15 threshold was implemented to discard

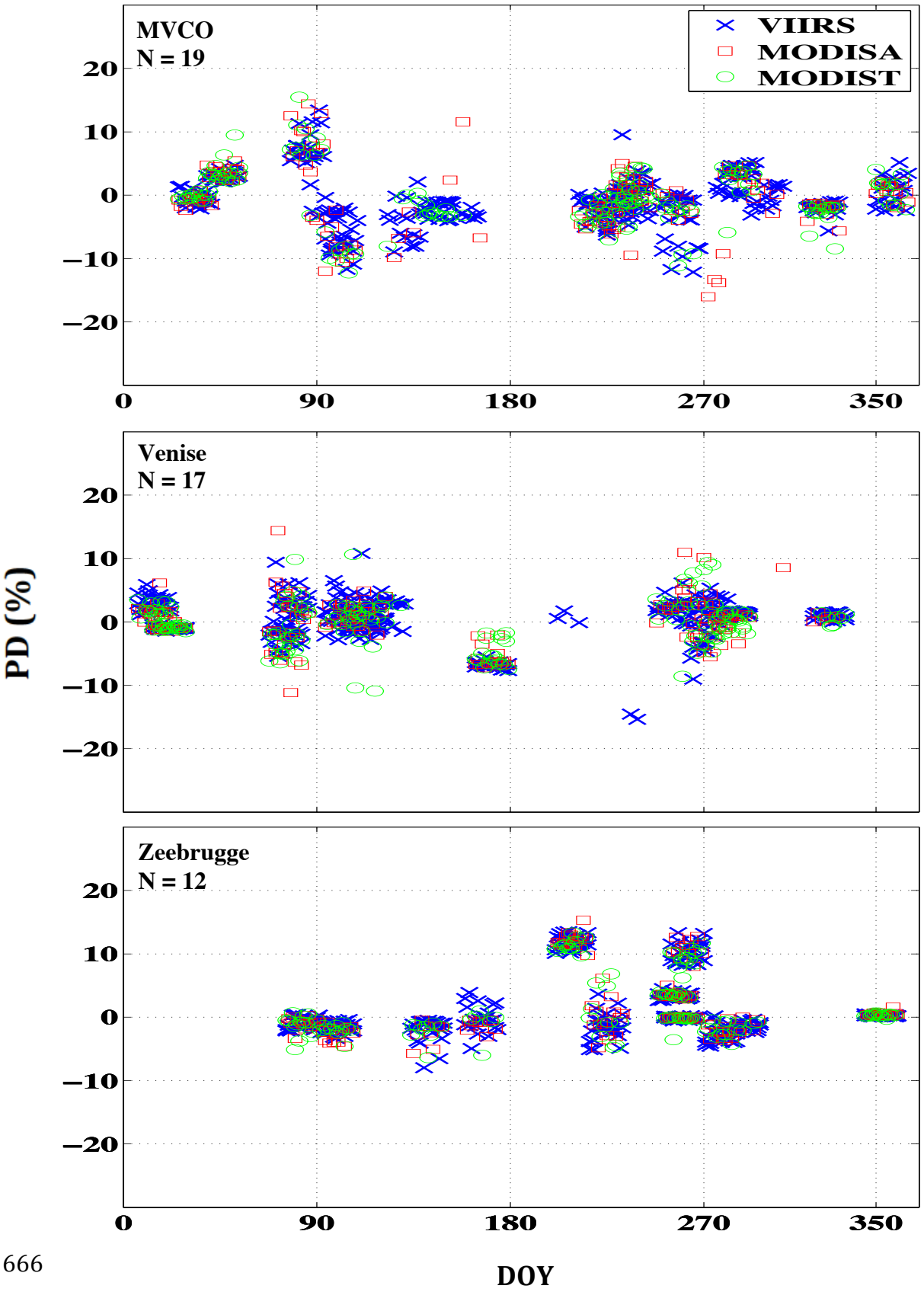

666

Fig. 9. The simulated percent differences (PD) for $\boldsymbol{R_{rs}(443)}$ (Eq. 8) shown for the three AERONET-OC stations for all available OLI scenes (N) at the sites. The PDs are calculated for **3×3** simulated OC pixels and a representative OLI OC pixel. The PD ranges from -20% to +30% for these sites and is mainly dependent on the environmental conditions (in-water features) captured by the OLI scene. The MODISA and MODIST show more day-today variability with respect to VIIRS.

667 simulated outliers, the daily simulated PDs (Eq. 8) can reach as high as ±18%. The
668 largest PDs may be attributed to influxes of terrestrial inputs and algal bloom events.
669 Second, MODISA and MODIST exhibit larger day-to-day variability in PD (vertical
670 axes) than that for VIIRS during an orbit cycle for most of the coastal conditions. The
671 per-orbit cycle variability of PD, on average, ranges from 1% to 15%. Third, spatial
672 variability around each site primarily drives the magnitude of the difference (note the
673 cluster of data points associated with each OLI scene). On the other hand, the variations
674 in viewing geometry result in a random variability (clutter) around the average PD. Note
675 that the PDs (or APDs) in the red channel are the largest (i.e., < 25%) amongst all the
676 channels due to the relatively small signal (Eq. 9).

677 This random variability in the day-to-day simulations is lowest for the MOBY and
678 BOUSSOLE sites. Fig. 10 illustrates variability for different orbits for six (A to F) OLI
679 scenes at the MOBY site. To comply with the existing calibration protocols of ocean
680 color products at the MOBY site (Bailey and Werdell 2006), the median of simulated
681 ocean color observations are computed within 5×5-element windows and compared
682 against representative OLI pixels (Section 2.3). For the scenes A, B, and C, the mean PD
683 is nearly zero with some random variability from orbit to orbit. The random variability
684 (around the mean trend) ranges from 0.5% to 1.5%. In general, VIIRS exhibits less
685 variability relative to MODISA and MODIST, in particular when spatial variability
686 around the site increases (e.g., scene E). The overall (mean) trend generally remains
687 within the ±5% range. The differences found for the BOUSSOLE site (not shown here)
688 range within ±4%. It is thus worthwhile noting that the variations in the footprint size

689 increase uncertainties (random variability) and may introduce bias in
690 calibration/validation efforts at these spatially homogenous sites.

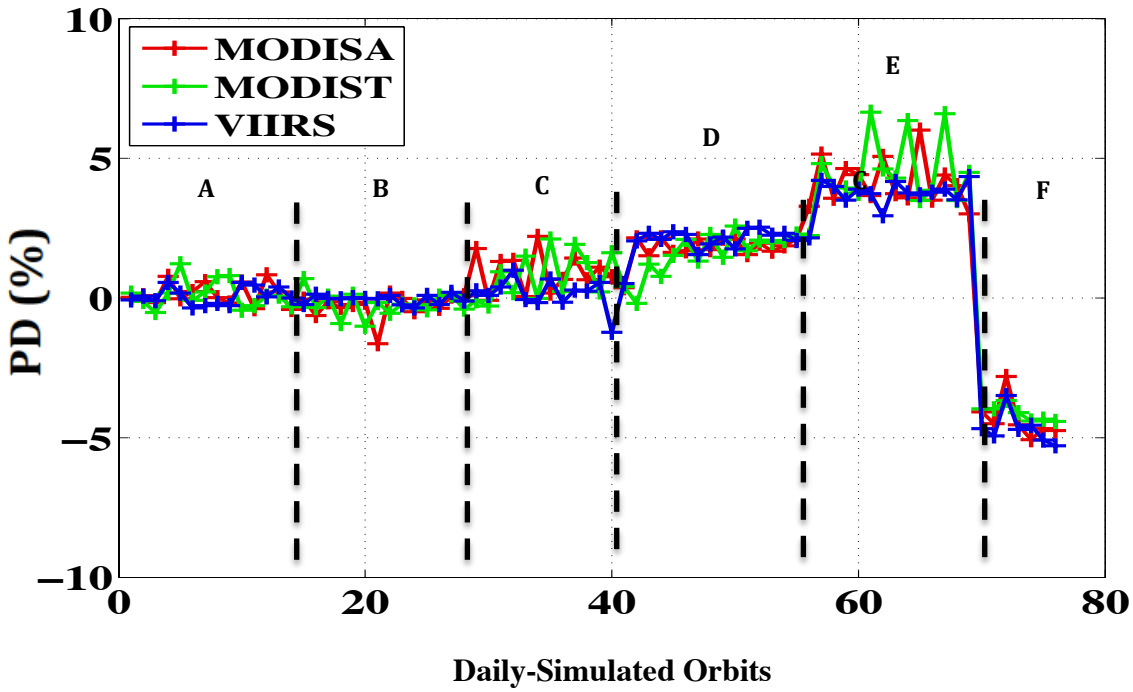

691

Fig. 10. The PD (%) shown for three OLI-derived R_{rs} (443) products (i.e., A, B, C, D, E, and F) for the MOBY site. The curves correspond to MODISA (red), MODIST (green), and VIIRS (blue) products. The solid lines denote PDs corresponding to **5×5** windows. The larger variability associated with MODIST and MODISA with respect to VIIRS is noticeable.

692

693

694

695

696

697

698

699

700

In the OC matchup analysis, after performing a multi-stage filtering (Bailey and Werdell 2006), the uncertainties are commonly attributed to the sensor calibration (at a reference wavelength), and radiative transfer modeling (atmospheric correction), as well as atmospheric conditions. Temporal averaging, however, diminishes impacts of spatial mismatch at validation sites (Bailey et al. 2008; Franz et al. 2007). To provide insights into the overall expected biases for the coastal sites for matchup analysis, we present average statistics derived from the metrics defined in Section 2.3. After discarding all the outliers (i.e., flagged simulated OC observations), 1091, 1084, and 2043 valid "matchups" were incorporated in this statistical analysis for MODISA, MODIST, and VIIRS, respectively. Fig. 11 illustrates the average absolute differences (APDs) for the 443nm channel. It is inferred that, on average, the APD (Eq. 9) increases with the increase in the window size at these coastal sites. This is expected as larger spatial variability is introduced in the matchup analysis by incorporating more OC observations in coastal waters. Compromise has to be made as increasing the window size lowers the noise contribution. Furthermore, there is, on average, 10-15% less difference associated with simulated matchups for VIIRS when compared to those of MODISA and MODIST. Although use of a single (center) pixel gives rise to a minimum difference in our simulated matchup analysis, in practice, residual detector striping/banding adds another source of uncertainty in the analysis. Thus, depending on the instrument performance (or the efficiency of the de-striping approach) and the environmental conditions (turbidity, resuspension, river plumes, algal blooms, etc.) either center pixel (1×1) or the

724 median/mean of a 3×3 window is recommended for use. Currently, the use of a 3×3-
725 element window is common practice for validating ocean color products in coastal waters
726 (Zibordi et al. 2009a). Although an apparent random variability is expected for

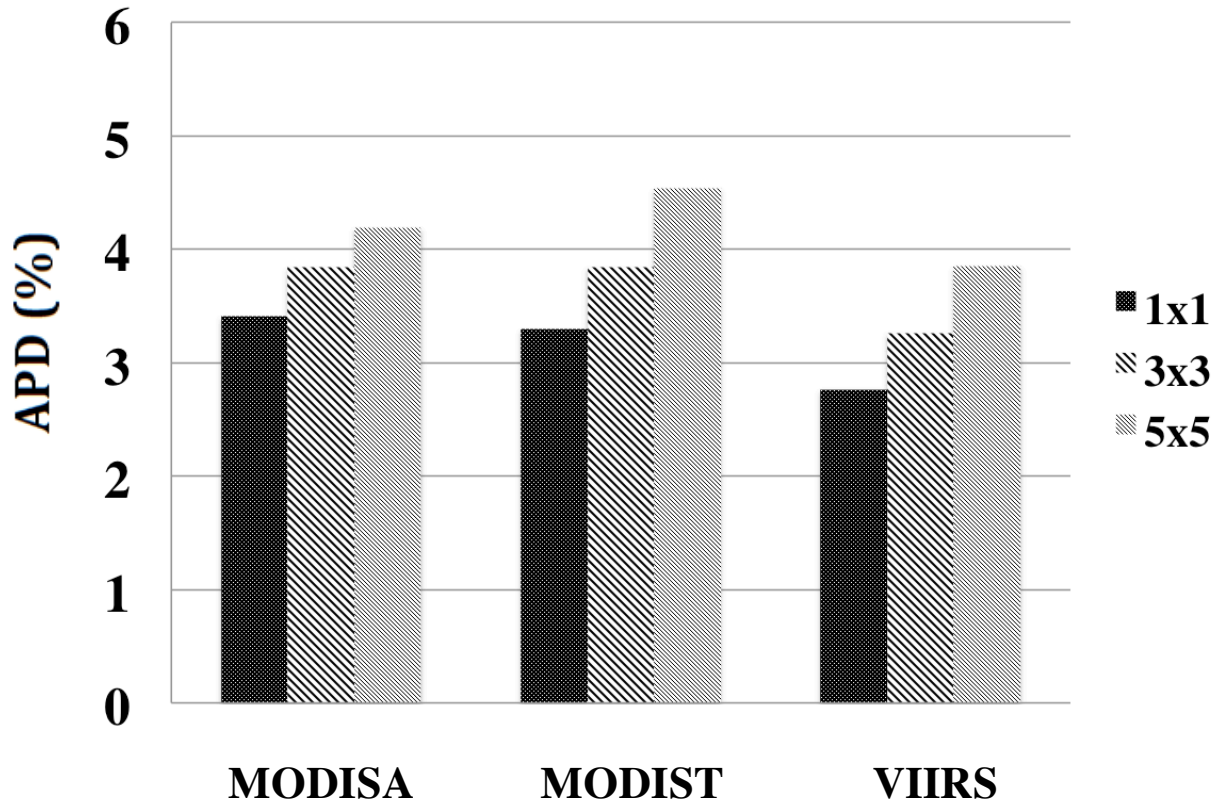

727

Fig. 11. The overall mean absolute differences (APDs) computed for simulated MODISA (N=1091), MODIST (N=1084), and VIIRS (N=2043) for different window sizes shown for the OLI 443nm channel. The windows are centered over the AERONET-OC (costal) sites.

728

729

730

731

732

733

Table 2. The average, per-band statistics computed for all the AERONET-OC (coastal) sites.

		1x1			3x3			5x5		
	Band (nm)	APD (%)	RMSD (1/sr)	PD (%)	APD (%)	RMSD (1/sr)	PD (%)	APD (%)	RMSD (1/sr)	PD (%)
MODISA	443	3.4	0.00024	0.8	3.8	0.00031	1	4.2	0.00033	1.4
	482	3.3	0.00029	0.7	3.7	0.00039	0.7	4.1	0.00043	1
	561	3.4	0.00040	0.6	4	0.00049	0.7	4.5	0.00055	1
	655	6.8	0.00038	0.6	8.1	0.00042	1.1	8.3	0.00047	1.9
MODIST	443	3.3	0.00023	0.8	3.8	0.00028	0.9	4.5	0.00036	1.6
	482	3.2	0.00027	0.6	3.7	0.00035	0.7	4.4	0.00045	1
	561	3.4	0.00037	0.5	4.3	0.00046	0.6	5.1	0.00056	1
	655	6.2	0.00038	1	8.4	0.00042	1.6	9	0.00049	1.4
VIIRS	443	2.8	0.00020	0.5	3.3	0.00027	0.6	3.8	0.00033	0.9
	482	2.7	0.00024	0.4	3.2	0.00034	0.6	3.8	0.00042	0.7
	561	2.9	0.00032	0.4	3.6	0.00045	0.6	4.3	0.00054	0.8
	655	5.6	0.00032	0.9	7.4	0.00041	1.8	8.6	0.00047	2.3

observations made from different orbits (Fig. 9) over varying environmental conditions (turbidity, resuspension, river plumes, etc.), we found that there is a bias that may not be removed by temporal averaging. At the coastal sites, the mean bias is found to be ~ 0.8%, which is the average of the mean difference, i.e., PD, derived for all the spectral bands and window sizes (Table 2). For the BOUSSOLE and MOBY sites, the temporally averaged PDs are found to fall within the ±0.1% range for the 443nm channel. The average PD, APD, and RMSD metrics are tabulated in Table 2. Note that these differences are attributed to matchup analysis at field stations where temporal averaging is possible. However, at in-situ sampling stations (taken during research cruises), the difference may be as high as ±18% (Fig. 9) depending on the footprint size and environmental conditions.

In addition to the overall expected differences, we also give insights into the mean variability, i.e., standard deviation around mean difference, shown along the y-axes of Figs. 9 for all the sites as a function of window size for the coastal sites. We found the uncertainty (variability) to be 3%, 3.5% and 3.9% for the 443nm channel, and 3%, 4.5%,

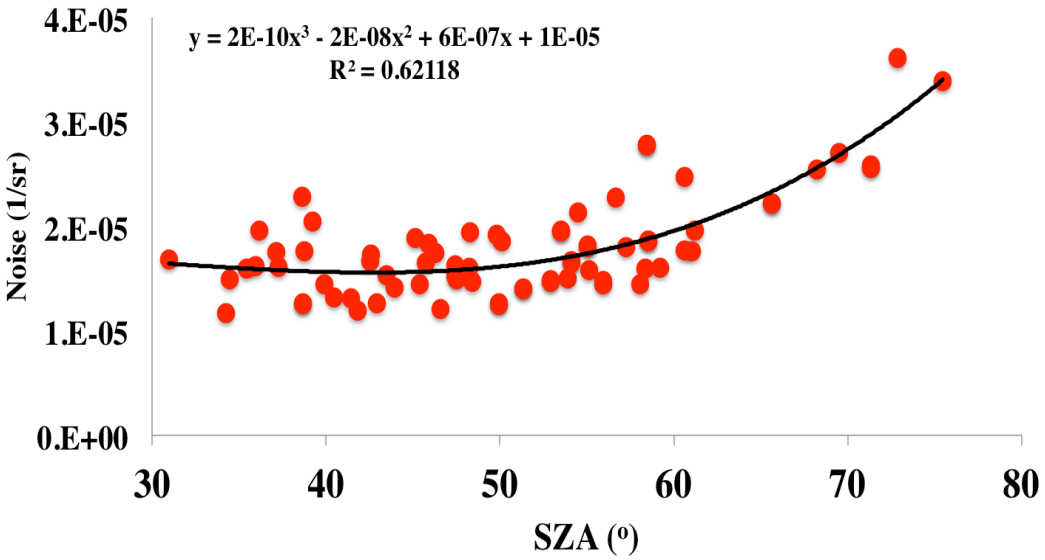

Fig. 12. The OLI-derived $R_{rs}(443)$ noise (1/sr) is shown as a function of solar zenith angle (SZA). The standard deviation was calculated over **5×5**-element windows over uniform bodies of water from various OLI scenes (N=75). The product noise remains relatively stable for low to

766 and 7.8% for the 561nm channel when 1×1, 3×3, and 5×5 windows are used
767 respectively. In contrast, the variability in PD (or APD) at the BOUSSOLE and MOBY
768 sites (located in blue waters) was reduced by increasing the window size, i.e., the 5×5-
769 element window provided minimum variability.

770 **4. DISCUSSIONS**

771 The basis of the spatial analysis presented here was the OLI-derived ocean color
772 products. Although OLI offers dramatically improved SNR when compared with the
773 previous Landsat sensors, the striping and banding effects limit the quality of the ocean
774 color products at the inherent 30-m resolution. This is, in particular, noticeable at lower
775 signal levels when solar zenith angle (SZA) is high. Fig. 12 illustrates the $R_{rs}(443)$ noise
776 as a function of SZA computed over uniform bodies of water across various independent
777 OLI-derived products. In order to surmount this instrument-induced variability within
778 OLI-derived products, the high-frequency components were removed by running a 3×3-
779 element window size. To evaluate the impact of the filtering, we conducted large-area
780 simulations (Section 3.1) for a handful of OLI scenes and found that the results (Table 1)
781 changed only by a fraction of a percent. The results presented in Section 3.2, however,
782 showed a more appreciable difference (< 5% in Table 2) for some of the coastal sites
783 located at higher latitudes where the impact of striping in OLI products was severe. These
784 scenes (characterized with low SNR) were therefore reprocessed with an average
785 Ångström exponent (derived over a subscene) to minimize the effects of striping.

786 The OLI scenes applied in Section 2.1 represents a large range of productivity/
787 turbidity ($0 < [Chla] < 15\ mg/m^3$) from Amazon River basin, Mississippi River and
788 Bay of Bengal to the Great Lakes. Our assumptions (e.g., use of a single sampling

789 function for MODIS across all channels; Fig. 2) in the simulation process have no
790 significant effects on the results. This was examined using a slightly different PSF over
791 three OLI scenes. The average APDs presented in Section 3.1 provide average estimates
792 for an overall error budget analysis when comparing gridded ocean color products at 1km
793 resolution. However, as discussed in Section 3.1, the actual per-pixel discrepancies may
794 differ depending on in-water features and viewing geometries.

795 Although the differences (Section 3.2) were found to reach up to ~18% in the blue-
796 green channels, the spatial mismatch in different (OLI) channels tend to agree in their
797 signs (Table 2) implying that even at highly spatially variable sites the impact on the
798 ocean color products derived from band-ratio algorithms (e.g., [Chla]) are expected to be
799 minimal. Note, however, that this does not hold true for all cases studied here, i.e., 10-
800 20% of the simulated matchups showed contradictory trends. The average statistics
801 (Table 2) extracted from more than 100 OLI scenes over six different coastal sites
802 provide a set of robust estimates for error budget analysis in ocean color product
803 validation chain in coastal waters. While the revisit cycle of these polar orbiters (SNPP,
804 Aqua, and Terra) similarly repeats every 16 days, we conducted a sensitivity study on the
805 choice of the orbit cycle where DOY=5 through DOY=20 orbits of Aqua-MODIS was
806 utilized for simulations over the MVCO site. The overall APD at the site changed only on
807 the order of 0.1% indicating that the choice of the 16-day orbit cycle is insignificant.

808 **5. CONCLUSIONS**

809 This study presents a novel, comprehensive approach to characterize the uncertainties
810 associated with the product intercomparisons and in-situ validation efforts induced by
811 different spatial sampling effects of three OC imagers. The high quality, moderate-

812 resolution (~30m) OLI-derived OC products obtained over various regions/locations are
813 central to the results presented here. Here, we emphasize the critical conclusions of the
814 study.

815 The following conclusions can be drawn from the results pertaining to the product
816 intercomparisons at regional scales:

817 • Due to the differences in the spatial sampling schemes of MODISA and VIIRS, there
818 is a viewing-angle (footprint-size) dependency on the product intercomparisons.
819 Therefore, care must be taken when high-fidelity per-pixel intercomparison is
820 desired.
821 • The mean absolute percent differences (APD) in product intercomparisons due to the
822 differences in the spatial sampling are estimated to be 1.8%, 1.9%, 2.4%, 4.3%,
823 2.7%, 1.8%, and 4% for the $R_{rs}(443)$, $R_{rs}(482)$, $R_{rs}(561)$, $R_{rs}(655)$, [Chla], $K_d(490)$,
824 and $b_{bp}(655)$ products, respectively.
825 • The differences in the products in the offshore regions are mitigated if a pair of
826 products is smoothed over window sizes of at least $7km \times 7km$.

827 The radiometric differences at coastal in-situ sites always include some level of
828 uncertainty in the spatial representativeness of the site. With the strategies set forth here,
829 we provide the following conclusions to give insights into the magnitude of these
830 uncertainties:

831 • The ocean color observation centered on the stationary in-situ coastal sites provides
832 the minimum temporally averaged bias and variability. Assuming residual
833 striping/banding effects in the products, a 3×3-element window is recommended.

834 On the other hand, 5×5-element boxes yield both lower biases and uncertainties
835 over clear open waters.
836 • The contribution of spatial sampling to differences between satellite and in-situ
837 measurements in near-shore areas can reach as large as 18%. This varies according
838 to the in-water spatial variability and the satellite orbit, which determines the
839 footprint size (sensor viewing angle).
840 • The APD in the spatial representativeness of a field site (for R_{rs} products) is found,
841 on average, to be 3.7%, 3.5%, 3.9%, 8.3% for the 443, 482, 561, and 655nm
842 channels, respectively.
843 • The daily observations of VIIRS show less random variability (induced by spatial
844 sampling) than those of MODISA and MODIST at the calibration sites (e.g.,
845 MOBY) as well as the coastal validation sites. In addition, the number of valid
846 simulated matchups for VIIRS was found twice larger than that of MODIS
847 suggesting that more robust statistical analysis is possible for the VIIRS products.
848 The results of this study, for the first time, allow for taking one step forward for a full
849 quantification of the overall error budget analysis of coastal ocean products by isolating
850 the errors associated with spatial sampling. Similar sensitivity analyses can be performed
851 to estimate uncertainties/biases in spectral sampling and geolocation errors to further
852 decompose the overall error budget. We further highlight the advantages of near-uniform
853 along-scan spatial sampling (assuming no loss in the radiometric performance) for future
854 ocean color missions like the Pre-Aerosol, Cloud, and ocean Ecosystem (PACE) and the
855 planned GEOstationary Coastal and Air Pollution Events (GEO-CAPE) to enhance our

ability in validating products and quantifying corresponding uncertainties for reliable monitoring of the changing coastal waters.

Acknowledgement

Financial support by the Geo-CAPE program at the NASA headquarters and support from Antonio Mannino with the NASA Ocean Biology Processing Group (OBPG) are greatly appreciated. We are also grateful to Robert E. Wolfe and Gary Lin with NASA GSFC's Terrestrial Information Systems Lab for the discussions of spatial performance of VIIRS and MODIS instruments. The computing support at the Terrestrial Information Systems Lab by Miguel O. Román and Ed Masuoka is acknowledged. We are also grateful to the anonymous reviewers for their thoughtful comments that help improve this manuscript.

References

Allen, J.I., Smyth, T.J., Siddorn, J.R., & Holt, M. (2008). How well can we forecast high biomass algal bloom events in a eutrophic coastal sea? *Harmful Algae, 8*, 70-76

Antoine, D., d'Ortenzio, F., Hooker, S.B., Bécu, G., Gentili, B., Tailliez, D., & Scott, A.J. (2008a). Assessment of uncertainty in the ocean reflectance determined by three satellite ocean color sensors (MERIS, SeaWiFS and MODIS-A) at an offshore site in the Mediterranean Sea (BOUSSOLE project). *Journal of Geophysical Research: Oceans, 113*

Antoine, D., Guevel, P., Deste, J.-F., Bécu, G., Louis, F., Scott, A.J., & Bardey, P. (2008b). The "BOUSSOLE" buoy-a new transparent-to-swell taut mooring dedicated to marine optics: Design, tests, and performance at sea. *Journal of Atmospheric and Oceanic Technology, 25*, 968-989

Bailey, S.W., Franz, B.A., & Werdell, P.J. (2010). Estimation of near-infrared water-leaving reflectance for satellite ocean color data processing. *Optics express, 18*, 7521-7527

Bailey, S.W., Hooker, S.B., Antoine, D., Franz, B.A., & Werdell, P.J. (2008). Sources and assumptions for the vicarious calibration of ocean color satellite observations. *Applied Optics, 47*, 2035-2045

Bailey, S.W., & Werdell, P.J. (2006). A multi-sensor approach for the on-orbit validation of ocean color satellite data products. *Remote Sensing of Environment, 102*, 12-23

886 Baker, N. (2011). VIIRS Geolocation Algorithm Theoretical Basis Document (ATBD). In. Goddard
887 Space Flight Center, Greenbelt, MD: Joint Polar Satellite System (JPPS)

888 Barnes, B.B., & Hu, C. (2015). Cross-Sensor Continuity of Satellite-Derived Water Clarity in the Gulf
889 of Mexico: Insights Into Temporal Aliasing and Implications for Long-Term Water Clarity Assessment.
890 *Geoscience and Remote Sensing, IEEE Transactions on, 53*, 1761-1772

891 Barnes, W.L., Pagano, T.S., & Salomonson, V.V. (1998). Prelaunch characteristics of the moderate
892 resolution imaging spectroradiometer (MODIS) on EOS-AM1. *Geoscience and Remote Sensing, IEEE*
893 *Transactions on, 36*, 1088-1100

894 Campbell, J.W., Blaisdell, J.M., & Darzi, M. (1996). Level-3 Sea WiFS data products: spatial and
895 temporal binning algorithms. *Oceanographic Literature Review, 9*, 952

896 Cao, C., De Luccia, F.J., Xiong, X., Wolfe, R., & Weng, F. (2014). Early on-orbit performance of the
897 visible infrared imaging radiometer suite onboard the suomi national polar-orbiting Partnership (S-NPP)
898 satellite. *Geoscience and Remote Sensing, IEEE Transactions on, 52*, 1142-1156

899 Cao, C., Xiong, J., Blonski, S., Liu, Q., Uprety, S., Shao, X., Bai, Y., & Weng, F. (2013). Suomi NPP
900 VIIRS sensor data record verification, validation, and long-term performance monitoring. *Journal of*
901 *Geophysical Research: Atmospheres, 118*, 11,664-611,678

902 Chander, G., Hewison, T.J., Fox, N., Wu, X., Xiong, X., & Blackwell, W.J. (2013). Overview of
903 intercalibration of satellite instruments. *Ieee Transactions on Geoscience and Remote Sensing, 51*, 1056-
904 1080

905 Clark, D., Gordon, H., Voss, K., Ge, Y., Broenkow, W., & Trees, C. (1997). Validation of atmospheric
906 correction over the oceans. *Journal of Geophysical Research: Atmospheres (1984–2012), 102*, 17209-
907 17217

908 Esaias, W.E., Abbott, M.R., Barton, I., Brown, O.B., Campbell, J.W., Carder, K.L., Clark, D.K., Evans,
909 R.H., Hoge, F.E., & Gordon, H.R. (1998). An overview of MODIS capabilities for ocean science
910 observations. *Geoscience and Remote Sensing, IEEE Transactions on, 36*, 1250-1265

911 Franz, B.A., Bailey, S.W., Kuring, N., & Werdell, P.J. (2015). Ocean color measurements with the
912 Operational Land Imager on Landsat-8: implementation and evaluation in SeaDAS. *Journal of Applied*
913 *Remote Sensing, 9*, 096070-096070

914 Franz, B.A., Bailey, S.W., Werdell, P.J., & McClain, C.R. (2007). Sensor-independent approach to the
915 vicarious calibration of satellite ocean color radiometry. *Applied Optics, 46*, 5068-5082

916 Franz, B.A., Werdell, P.J., Meister, G., Bailey, S.W., EpleeJr, R.E., Feldman, G.C., Kwiatkowskaa, E.,
917 McClain, C.R., Patt, F.S., & Thomas, D. (2005). The continuity of ocean color measurements from
918 SeaWiFS to MODIS. In, *Optics & Photonics 2005* (pp. 58820W-58820W-58813): International Society for
919 Optics and Photonics

920 Gerace, A.D., Schott, J.R., & Nevins, R. (2013). Increased potential to monitor water quality in the
921 near-shore environment with Landsat's next-generation satellite. *Journal of Applied Remote Sensing, 7*,
922 073558-073558

923 Gohin, F., Loyer, S., Lunven, M., Labry, C., Froidefond, J.-M., Delmas, D., Huret, M., & Herbland, A.
924 (2005). Satellite-derived parameters for biological modelling in coastal waters: Illustration over the eastern
925 continental shelf of the Bay of Biscay. *Remote Sensing of Environment, 95*, 29-46

Gordon, H.R. (1997). Atmospheric correction of ocean color imagery in the Earth Observing System era. *Journal of Geophysical Research: Atmospheres (1984–2012), 102*, 17081-17106

Holst, G.C. (2008). *Electro-optical Imaging System Performance*. (Fifth ed.). Bellingham JCD Buliding and SPIE

Hooker, S., Esaias, W., Feldman, G., Gregg, W., & McClain, C. (1992). In SB Hooker, & ER Firestone. *An overview of SeaWiFS and Ocean Color, NASA Tech. Memo, 104566*, 24

Hooker, S.B., & Maritorena, S. (2000). An evaluation of oceanographic radiometers and deployment methodologies. *Journal of Atmospheric and Oceanic Technology, 17*, 811-830

Hu, C., Feng, L., & Lee, Z. (2013). Uncertainties of SeaWiFS and MODIS remote sensing reflectance: Implications from clear water measurements. *Remote Sensing of Environment, 133*, 168-182

Hu, C., & Le, C. (2014). Ocean color continuity from VIIRS measurements over Tampa Bay. *Geoscience and Remote Sensing Letters, IEEE, 11*, 945-949

IOCCG (1997). Ocean-colour data merging. In W.W.A. Gregg, J., Kwiatkowska, E., Maritorena, S., Mélin, F., Murakami, H., Pinnock, S., Pottier,C. (Ed.), *Reports of the International Ocean Colour Coordinating Group* (p. 68). Dartmouth, Canada: IOCCG

Irons, J.R., Dwyer, J.L., & Barsi, J.A. (2012). The next Landsat satellite: The Landsat Data Continuity Mission. *Remote Sensing of Environment, 122*, 11-21

Ladner, S., Arnone, R., Vandermeulen, R., Martinolich, P., Lawson, A., Bowers, J., Crout, R., Ondrusek, M., & Fargion, G. (2014). Inter-satellite comparison and evaluation of navy Suomi-NPP VIIRS and MODIS-Aqua ocean color properties. In, *SPIE Sensing Technology+ Applications* (pp. 911107-911107-911109): International Society for Optics and Photonics

Lee, Z., Arnone, R., Hu, C., Werdell, P.J., & Lubac, B. (2010). Uncertainties of optical parameters and their propagations in an analytical ocean color inversion algorithm. *Applied Optics, 49*, 369-381

Lee, Z., Hu, C., Arnone, R., & Liu, Z. (2012). Impact of sub-pixel variations on ocean color remote sensing products. *Optics express, 20*, 20844-20854

Lee, Z.P., Carder, K.L., & Arnone, R.A. (2002). Deriving inherent optical properties from water color: a multiband quasi-analytical algorithm for optically deep waters. *Applied Optics, 41*, 5755-5772

Lin, G., Tilton, J.C., Wolfe, R.E., Tewari, K.P., & Nishihama, M. (2013). SNPP VIIRS spectral bands co-registration and spatial response characterization. In J. J. Butler, X. Xiong, & X. Gu (Eds.), *Earth Observing Systems XVIII* (pp. 88661G-88661G-88615). San Diego: SPIE

Maritorena, S., d'Andon, O.H.F., Mangin, A., & Siegel, D.A. (2010). Merged satellite ocean color data products using a bio-optical model: Characteristics, benefits and issues. *Remote Sensing of Environment, 114*, 1791-1804

Maritorena, S., & Siegel, D.A. (2005). Consistent merging of satellite ocean color data sets using a bio-optical model. *Remote Sensing of Environment, 94*, 429-440

McClain, C.R., Feldman, G.C., & Hooker, S.B. (2004). An overview of the SeaWiFS project and strategies for producing a climate research quality global ocean bio-optical time series. *Deep Sea Research Part II: Topical Studies in Oceanography, 51*, 5-42

McGranahan, G., Balk, D., & Anderson, B. (2007). The rising tide: assessing the risks of climate change and human settlements in low elevation coastal zones. *Environment and urbanization, 19*, 17-37

Meister, G., Franz, B., Kwiatkowska, E.J., & McClain, C.R. (2012). Corrections to the calibration of MODIS Aqua ocean color bands derived from SeaWiFS data. *Geoscience and Remote Sensing, IEEE Transactions on, 50*, 310-319

Meister, G., & McClain, C.R. (2010). Point-spread function of the ocean color bands of the Moderate Resolution Imaging Spectroradiometer on Aqua. *Applied Optics, 49*, 6276-6285

Mélin, F., & Franz, B.A. (2014). Assessment of Satellite Ocean Colour Radiometry and Derived Geophysical Products. In C.D. G. Zibordi, A. Parr (Ed.), *Optical Radiometry for Ocean Climate Measurements, Experimental Methods in Physical Sciences* (pp. 609-632): Elsevier Academic Press.

Mélin, F., Vantrepotte, V., Clerici, M., D'Alimonte, D., Zibordi, G., Berthon, J.-F., & Canuti, E. (2011). Multi-sensor satellite time series of optical properties and chlorophyll-a concentration in the Adriatic Sea. *Progress in Oceanography, 91*, 229-244

Mélin, F., Zibordi, G., & Berthon, J.-F. (2007). Assessment of satellite ocean color products at a coastal site. *Remote Sensing of Environment, 110*, 192-215

Mélin, F., Zibordi, G., & Djavidnia, S. (2009). Merged series of normalized water leaving radiances obtained from multiple satellite missions for the Mediterranean Sea. *Advances in Space Research, 43*, 423-437

Moore, T.S., Campbell, J.W., & Feng, H. (2015). Characterizing the uncertainties in spectral remote sensing reflectance for SeaWiFS and MODIS-Aqua based on global in situ matchup data sets. *Remote Sensing of Environment, 159*, 14-27

Morel, A., Antoine, D., & Gentili, B. (2002). Bidirectional Reflectance of Oceanic Waters: Accounting for Raman Emission and Varying Particle Scattering Phase Function. *Applied Optics, 41*, 6289-6306

Morel, A., & Gentili, B. (1996). Diffuse reflectance of oceanic waters. III. Implication of bidirectionality for the remote-sensing problem. *Applied Optics, 35*, 4850-4862

Mueller, J.L. (2000). SeaWiFS algorithm for the diffuse attenuation coefficient, K (490), using water-leaving radiances at 490 and 555 nm. *SeaWiFS postlaunch calibration and validation analyses, part, 3*, 24-27

Mueller, J.L., Fargion, G.S., McClain, C.R., Mueller, J., Brown, S., Clark, D., Johnson, B., Yoon, H., Lykke, K., & Flora, S. (2004). Ocean Optics Protocols For Satellite Ocean Color Sensor Validation, Revision 5, Volume VI: Special Topics in Ocean Optics Protocols, Part 2. In: NASA Report 211621, 2003, 1-36

Müller, D., Krasemann, H., Brewin, R.J., Brockmann, C., Deschamps, P.-Y., Doerffer, R., Fomferra, N., Franz, B.A., Grant, M.G., & Groom, S.B. (2015). The Ocean Colour Climate Change Initiative: II. Spatial and temporal homogeneity of satellite data retrieval due to systematic effects in atmospheric correction processors. *Remote Sensing of Environment, 162*, 257-270

Natvik, L.-J., & Evensen, G. (2003). Assimilation of ocean colour data into a biochemical model of the North Atlantic: Part 1. Data assimilation experiments. *Journal of Marine Systems, 40*, 127-153

Nixon, S.W. (1995). Coastal marine eutrophication: a definition, social causes, and future concerns. *Ophelia, 41*, 199-219

O'Reilly, J.E., Maritorena, S., Mitchell, B.G., Siegel, D.A., Carder, K.L., Garver, S.A., Kahru, M., & McClain, C. (1998). Ocean color chlorophyll algorithms for SeaWiFS. *Journal of Geophysical Research: Oceans (1978–2012), 103*, 24937-24953

O'Reilly, J.E., Maritorena, S., Siegel, D.A., O'Brien, M.C., Toole, D., Mitchell, B.G., Kahru, M., Chavez, F.P., Strutton, P., & Cota, G.F. (2000). Ocean color chlorophyll a algorithms for SeaWiFS, OC2, and OC4: Version 4. *SeaWiFS postlaunch calibration and validation analyses, part, 3*, 9-23

Ouillon, S., Douillet, P., & Andréfouët, S. (2004). Coupling satellite data with in situ measurements and numerical modeling to study fine suspended-sediment transport: a study for the lagoon of New Caledonia. *Coral Reefs, 23*, 109-122

Pahlevan, N., Lee, Z., Wei, J., Schaff, C., Schott, J., & Berk, A. (2014). On-orbit radiometric characterization of OLI (Landsat-8) for applications in aquatic remote sensing. *Remote Sensing of Environment, 154*, 272–284

Pahlevan, N., & Schott, J.R. (2013). Leveraging EO-1 to Evaluate Capability of New Generation of Landsat Sensors for Coastal/Inland Water Studies. *Selected Topics in Applied Earth Observations and Remote Sensing, IEEE Journal of, 6*, 360-374

Schott, J.R. (2007). *Remote Sensing The Image Chain Approach*. (2nd ed.). New York: Oxford Unversity Press

Schowengerdt, R.A. (1997). *Remote Sensing: Models and Methods for Image Processing*. (2nd ed.). Chesnutt Hill, MA: Academic Press

Storey, J., Choate, M., & Lee, K. (2014). Landsat 8 Operational Land Imager on-orbit geometric calibration and performance. *Remote Sensing, 6*, 11127-11152

Vanhellemont, Q., & Ruddick, K. (2014). Turbid wakes associated with offshore wind turbines observed with Landsat 8. *Remote Sensing of Environment, 145*, 105-115

Vanhellemont, Q., & Ruddick, K. (2015). Advantages of high quality SWIR bands for ocean colour processing: Examples from Landsat-8. *Remote Sensing of Environment, 161*, 89-106

Vitousek, P.M., Mooney, H.A., Lubchenco, J., & Melillo, J.M. (1997). Human domination of Earth's ecosystems. *Science, 277*, 494-499

Vörösmarty, C.J., Green, P., Salisbury, J., & Lammers, R.B. (2000). Global water resources: vulnerability from climate change and population growth. *Science, 289*, 284-288

Wang, M. (1999). A sensitivity study of the SeaWiFS atmospheric correction algorithm: Effects of spectral band variations. *Remote Sensing of Environment, 67*, 348-359

Wang, P., Boss, E.S., & Roesler, C. (2005). Uncertainties of inherent optical properties obtained from semianalytical inversions of ocean color. *Applied Optics, 44*, 4074-4085

Wolfe, R.E., Lin, G., Nishihama, M., Tewari, K.P., Tilton, J.C., & Isaacman, A.R. (2013). Suomi NPP VIIRS prelaunch and on-orbit geometric calibration and characterization. *Journal of Geophysical Research: Atmospheres, 118*, 11,508-511,521

Wolfe, R.E., Nishihama, M., Fleig, A.J., Kuyper, J.A., Roy, D.P., Storey, J.C., & Patt, F.S. (2002). Achieving sub-pixel geolocation accuracy in support of MODIS land science. *Remote Sensing of Environment, 83*, 31-49

Wolfe, R.E., Roy, D.P., & Vermote, E. (1998). MODIS land data storage, gridding, and compositing methodology: Level 2 grid. *Geoscience and Remote Sensing, IEEE Transactions on, 36*, 1324-1338

Xiong, X., Che, N., & Barnes, W. (2006). Terra MODIS on-orbit spectral characterization and performance. *Geoscience and Remote Sensing, IEEE Transactions on, 44*, 2198-2206

Xiong, X., Sun, J., Xiong, S., & Barnes, W.L. (2004). Using the moon for MODIS on-orbit spatial characterization. In (pp. 480-487)

Zibordi, G., Berthon, J.-F., Mélin, F., D'Alimonte, D., & Kaitala, S. (2009a). Validation of satellite ocean color primary products at optically complex coastal sites: Northern Adriatic Sea, Northern Baltic Proper and Gulf of Finland. *Remote Sensing of Environment, 113*, 2574-2591

Zibordi, G., Mélin, F., & Berthon, J.-F. (2012). Intra-annual variations of biases in remote sensing primary ocean color products at a coastal site. *Remote Sensing of Environment, 124*, 627-636

Zibordi, G., Mélin, F., Berthon, J.-F., Holben, B., Slutsker, I., Giles, D., D'Alimonte, D., Vandemark, D., Feng, H., & Schuster, G. (2009b). AERONET-OC: a network for the validation of ocean color primary products. *Journal of Atmospheric and Oceanic Technology, 26*, 1634-1651

Zibordi, G., Mélin, F., & Berthon, J.F. (2006). Comparison of SeaWiFS, MODIS and MERIS radiometric products at a coastal site. *Geophysical Research Letters, 33*

Zibordi, G., Mélin, F., Hooker, S.B., D'Alimonte, D., & Holben, B. (2004). An autonomous above-water system for the validation of ocean color radiance data. *Geoscience and Remote Sensing, IEEE Transactions on, 42*, 401-415

Zibordi, G., Mélin, F., Voss, K.J., Johnson, B.C., Franz, B.A., Kwiatkowska, E., Huot, J.-P., Wang, M., & Antoine, D. (2015). System vicarious calibration for ocean color climate change applications: Requirements for in situ data. *Remote Sensing of Environment, 159*, 361-369

Appendix

Table A1. The OLI scenes processed for the product intercomparison study (Section 2.1) are tabulated

LC80090262014248LGN00	LC80440342014285LGN00	LC81370452015076LGN00
LC80110302013227LGN00	LC80440352015064LGN00	LC81640402014310LGN00
LC80110322014086LGN00	LC80450342014276LGN00	LC81650392015064LGN00
LC80130322014100LGN00	LC80790152014210LGN00	LC81910212014115LGN00
LC80140372014299LGN00	LC80790162014210LGN00	LC81910292013208LGN00
LC80170302014096LGN00	LC80840122015168LGN00	LC81910292013224LGN00
LC80190312014270LGN00	LC80840132015168LGN00	LC81980222014068LGN00
LC80190402014046LGN00	LC81180372015071LGN00	LC82240592013327LGN00
LC80210402015079LGN00	LC81180392013241LGN00	LC82250582014225LGN00
LC80440342014109LGN00	LC81360452015069LGN00	

List of Figures

(N=75). The product noise remains relatively stable for low to medium range SZA but increases beyond SZA=**58**°.